

Cite this: *Chem. Sci.*, 2021, 12, 15802

All publication charges for this article have been paid for by the Royal Society of Chemistry

# Active site engineering of single-atom carbonaceous electrocatalysts for the oxygen reduction reaction

Guangbo Chen,<sup>a</sup> Haixia Zhong<sup>a</sup> and Xinliang Feng<sup>a,b\*</sup>

The electrocatalytic oxygen reduction reaction (ORR) is the vital process at the cathode of next-generation electrochemical storage and conversion technologies, such as metal–air batteries and fuel cells. Single-metal-atom and nitrogen co-doped carbonaceous electrocatalysts (M–N–C) have emerged as attractive alternatives to noble-metal platinum for catalyzing the kinetically sluggish ORR due to their high electrical conductivity, large surface area, and structural tunability at the atomic level, however, their application is limited by the low intrinsic activity of the metal–nitrogen coordination sites (M–N<sub>x</sub>) and inferior site density. In this Perspective, we summarize the recent progress and milestones relating to the active site engineering of single atom carbonous electrocatalysts for enhancing the ORR activity. Particular emphasis is placed on the emerging strategies for regulating the electronic structure of the single metal site and populating the site density. In addition, challenges and perspectives are provided regarding the future development of single atom carbonous electrocatalysts for the ORR and their utilization in practical use.

Received 22nd October 2021  
Accepted 10th November 2021

DOI: 10.1039/d1sc05867c

rsc.li/chemical-science

<sup>a</sup>Center for Advancing Electronics Dresden (cfaed) and Faculty of Chemistry and Food Chemistry, Technische Universität Dresden, Mommsenstr. 4, 01062 Dresden, Germany. E-mail: xinliang.feng@tu-dresden.de

<sup>b</sup>Department of Synthetic Materials and Functional Devices, Max Planck Institute of Microstructure Physics, Weinberg 2, Halle (Saale), D-06120, Germany

## 1. Introduction

With the rapid depletion of fossil fuels and growing environmental concerns, electrochemical energy storage and conversion technologies have emerged as promising pathways for developing clean and sustainable energy devices.<sup>1,2</sup> The electrochemical oxygen reduction reaction (ORR) plays a significant role in determining the efficiency of next-generation energy



Guangbo Chen received his PhD degree in Chemistry from Technische Universität Dresden (TU Dresden) in 2021 under the supervision of Prof. Xinliang Feng. Thereafter, he continued his academic research as a post-doctoral fellow in the Chair of Molecular Functional Materials at TU Dresden. His research topic mainly focuses on the design and synthesis of carbonaceous and two-dimensional

based nanostructures for energy storage and conversion applications.



Xinliang Feng is a full professor and has been the head of the Chair for Molecular Functional Materials at TU Dresden since 2014. Starting from 2021, he has been the director of Max Planck Institute of Microstructure Physics, Germany. His current scientific interests include organic synthetic methodology, organic synthesis, and supramolecular chemistry of  $\pi$ -conjugated systems, bottom-up

synthesis of graphene and graphene nanoribbons, electrochemical exfoliation of 2D crystals, 2D polymers, and supramolecular polymers as well as 2D carbon-rich conjugated polymers for optoelectronic applications, energy storage and conversion, and new energy devices and technologies.



storage and conversion systems, *e.g.*, metal–air batteries and proton exchange membrane fuel cells (PEMFCs).<sup>3–5</sup> At the air cathode of metal–air batteries and PEMFCs, the O<sub>2</sub> molecules are reduced into OH<sup>−</sup> (in bases) and water (in acids) *via* a four proton-coupled electron transfer (PCET) pathway, respectively.<sup>6–10</sup> However, the four electrons, multi-O-containing intermediates (*i.e.*, OH\*, O\* and OOH\*), and three phases (*i.e.*, solid catalyst, liquid electrolyte and gaseous O<sub>2</sub>) involved in the process make the ORR kinetically sluggish with a large overpotential loss, calling for highly efficient ORR electrocatalysts.<sup>11–13</sup> Until now, platinum-group-metal (PGM)-based materials have been the benchmark electrocatalysts for catalyzing the ORR.<sup>14–17</sup> Unfortunately, the high cost, scarcity, and poor stability of PGMs seriously hamper their widespread utilization in practical energy systems.<sup>18–20</sup>

Compared to PGM-based catalysts, single-metal-atom and nitrogen co-doped carbonaceous (M–N–C) PGM-free materials have been regarded as emerging alternatives for catalyzing the ORR, attributed to their high electrical conductivity, large surface areas, and structural tunability at the atomic level.<sup>21–31</sup> In 1964, macrocyclic compounds, such as metal phthalocyanines, were initially found active toward the ORR.<sup>32</sup> Afterward, it was discovered that high-temperature pyrolysis could effectively enhance the ORR activity and durability of these macrocycle-derived catalysts.<sup>33,34</sup> These pioneering studies opened the window and inspired the widespread investigation of single atom carbonous materials as efficient ORR electrocatalysts. In the early 2000s, instead of expensive metal-macrocycles, common nitrogen-containing precursors, inorganic metal sources, and high-surface-area carbon supports were used to prepare M–N–C catalysts, which showed significantly promoted catalytic performance.<sup>35</sup> Since then, numerous synthetic strategies have been devoted to the preparation of M–N–C

electrocatalysts, through combining various N- and metal-containing precursors and careful optimization of the combinations and thermal treatments, resulting in highly variable coordination chemistry and densities of active sites and consequently drastically different ORR activities.<sup>36–39</sup> Time-of-flight secondary ion mass spectrometry (MS)-based investigations indicated that the FeN<sub>2</sub>C<sub>4</sub><sup>+</sup> ion was detected in all synthesized Fe–N–C electrocatalysts regardless of the Fe precursor or synthesis procedures used.<sup>40</sup> Thus, the catalytic site for the ORR in these Fe–N–C electrocatalysts was first proposed to be similar to the molecular structure of Fe–N<sub>x</sub> in an iron macrocyclic complex.<sup>41</sup>

With the prosperous development of M–N–C electrocatalysts, advanced characterization techniques have been adopted to identify the ORR active site.<sup>42–44</sup> Atomic-resolution aberration-corrected scanning transmission electron microscopy (AC-STEM) is a powerful technique to directly observe the distribution of single atoms and even obtain the atomic structure of active moieties.<sup>45</sup> In 2016, Zelenay *et al.* combined AC-STEM and electron energy-loss spectroscopy (EELS) to investigate the structure and composition of the active moieties in a (CM + PANI)–Fe–C electrocatalyst.<sup>46</sup> The coordination structure of individual Fe atoms could be clearly observed on the graphene sheet. The presence of N around the Fe was then confirmed by EELS, giving an average composition of Fe–N<sub>4</sub> by quantifying the ratio of Fe-to-N.

X-ray absorption spectroscopy (XAS) is another powerful tool to analyze the coordination environment around the metal center of M–N–C electrocatalysts.<sup>47</sup> Thereinto, X-ray absorption near edge structure (XANES) analysis reveals the metal valence state and uncovers the local atomic arrangement.<sup>48</sup> Further, extended X-ray absorption fine structure (EXAFS) analysis offers precise structural information including the coordination

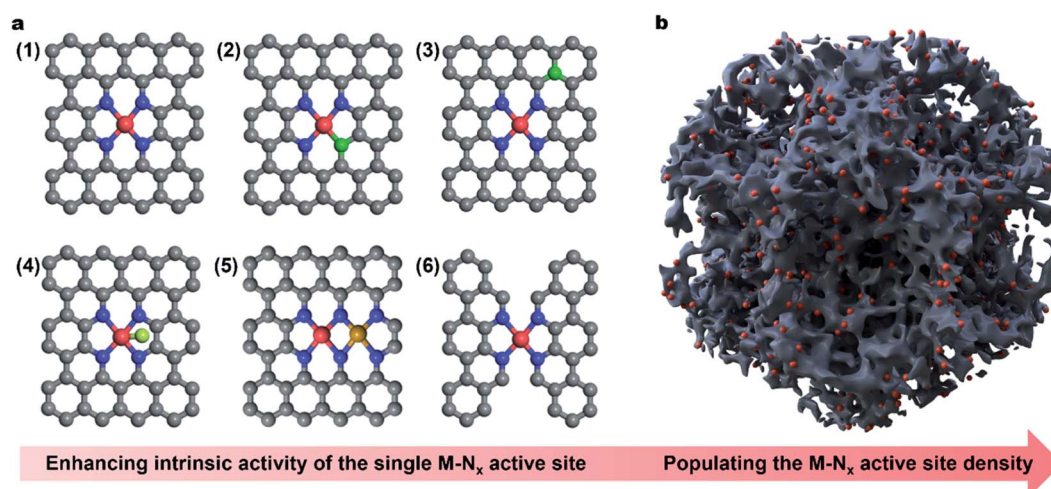


**Fig. 1** Schematic illustration of active engineering of single-atom carbonaceous M–N–C electrocatalysts for promoting the ORR activity. (a) Enhancing the intrinsic activity of the (1) single M–N<sub>x</sub> site *via* (2) regulation of the coordination geometry, (3) heteroatom incorporation, (4) axial ligand modification, (5) construction of dual-metal sites and (6) regulation of the carbon skeleton geometry. The brown, blue and red spheres represent C, N, and central M atoms, respectively. The green sphere stands for the heteroatom. The light green sphere represents the ligand on the M–N<sub>x</sub> site. The dark yellow sphere is the second metal site near the M–N<sub>x</sub>. (b) Populating the site density by engineering porous carbon structures.



number, and the bond distance between the central atom and neighboring atoms, which is widely used to identify the single atom characteristic of M–N–C electrocatalysts.<sup>49</sup> In 2015, Jaouen *et al.* utilized the XAS technique to investigate the active sites of Fe–N–C electrocatalysts on the basis of the successful synthesis of atomic Fe doped carbons.<sup>50</sup> The Fourier transforms of the EXAFS spectra indicated the absence of iron based crystalline structures. To further identify the active sites, the simulated XANES spectra were obtained and compared with the experimental results. By screening numerous possible structures, they found that FeN<sub>4</sub>C<sub>12</sub> was the most possible active moiety for the ORR. Similarly, single atomic cobalt (Co),<sup>25,51–54</sup> manganese (Mn),<sup>55–57</sup> zinc (Zn),<sup>58</sup> and copper (Cu)<sup>59,60</sup> were detected by XAS and visualized by AC-STEM in Co–N–C, Mn–N–C, Zn–N–C and Cu–N–C electrocatalysts, respectively, indicating that the active sites were M–N<sub>x</sub> (Fig. 1a).

The fruitful identification and insightful understanding of the M–N<sub>x</sub> active sites enabled the rational design and preparation of various efficient M–N–C electrocatalysts for the ORR *via* different synthetic approaches.<sup>61,62</sup> Currently, the representative synthetic strategies towards M–N–C electrocatalysts can be summarized as: (1) carbonization of metal-containing complexes or mixtures of specific precursors,<sup>63–66</sup> (2) carbonization of metal–organic frameworks (MOFs),<sup>67–72</sup> and (3) the template-assisted pyrolysis approach,<sup>73,74</sup> which can be seen in the recently published excellent review articles, examining both the design of M–N–C materials and their ORR activities.<sup>22,38,42,75–79</sup> Until now, M–N–C electrocatalysts have achieved outstanding ORR activity in alkaline solutions, exceeding that of the benchmark Pt/C catalyst.<sup>80</sup> The distinguished ORR activity of such M–N–C materials empowered the as-assembled metal–air batteries with superior performance.<sup>81</sup> Unfortunately, in an acidic electrolyte, the electrocatalytic activities of such M–N–C materials are still much lower than those of PGM-based components,<sup>82</sup> motivating the further rational engineering of the active site at the atomic level.

In this Perspective, we do not intend to be exhaustive but aim to highlight the latest achievements on the active site engineering of single atom carbonous electrocatalysts for the ORR. Especially, we summarize the representative approaches to enhancing the intrinsic activity of the (1) M–N<sub>x</sub> active site by modulating the electronic structure of the single metal sites, including (2) regulation of coordination geometry, (3) heteroatom incorporation (*e.g.*, sulphur (S), phosphorus (P) or boron (B) near the M atom), (4) axial ligand modification, (5) construction of dual-metal sites and (6) regulation of the carbon skeleton geometry (Fig. 1a). Besides, we present the recent progress in improving the mass activity *via* populating the site density by porosity engineering (Fig. 1b). Finally, challenges and perspectives are provided regarding the future development of single atom carbonaceous M–N–C electrocatalysts for the ORR and their applications in practical energy technology. We hope that this Perspective article will shed light on the development of highly efficient carbonaceous nanomaterials *via* rational active site engineering as alternative electrocatalysts to PGM-based systems, eventually realizing widespread applications in metal–air batteries and PEMFCs.

## 2. Engineering of the M–N<sub>x</sub> active site for enhancing the intrinsic activity

The central atom of various M–N–C electrocatalysts with different electronic structures will undoubtedly determine the ORR catalytic activity.<sup>83–85</sup> In the past decade, much progress has been made to reveal the intrinsic ORR activity of M–N–C electrocatalysts, following the order of Fe–N–C > Co–N–C > Cu–N–C > Mn–N–C > Ni–N–C.<sup>86–91</sup> Accordingly, the sections below will mainly focus on Fe–N–C systems, examining the strategies for enhancing their intrinsic activity. According to the Sabatier principle, the adsorption of ORR intermediates (*i.e.*, O<sub>2</sub><sup>\*</sup>, OOH<sup>\*</sup>, O<sup>\*</sup> and OH<sup>\*</sup>) on the active site should be neither too strong nor too weak.<sup>92</sup> Unfortunately, like benchmark Pt, the adsorption of ORR intermediates on the Fe–N<sub>x</sub> sites is still too strong, which seriously limits their desorption and then the ORR kinetics,<sup>93</sup> while on the Co–N<sub>x</sub> site, such adsorption energy is too weak, restricting the formation of corresponding intermediates.<sup>94</sup> Engineering the local geometry of the single metal site (*e.g.*, Fe or Co) can effectively modulate its electronic structure, hence optimizing the adsorption/desorption strength of O<sub>2</sub> and ORR intermediates and thus promoting the intrinsic activity.

### 2.1 Regulation of the coordination geometry of the metal center

In most of the M–N–C electrocatalysts, the central metal atom is coordinated by four N atoms, forming the M–N<sub>4</sub> coordination site.<sup>49</sup> For the Fe–N<sub>4</sub> coordination geometry, the N atoms can be typically classified into pyridinic- or pyrrolic-N.<sup>95</sup> Cao *et al.* proved that Fe@pyrrolic-N<sub>4</sub> presented higher ORR activity than Fe@pyridinic-N<sub>4</sub> by combining both experiments and density functional theory (DFT) calculations.<sup>96</sup> The same conclusion was also reported by Wu *et al.*<sup>97</sup> They constructed high-purity pyrrole-type Fe–N<sub>4</sub> (HP-Fe–N<sub>4</sub>) by a simple ammonia-assisted strategy and compared its performance with pyridine-type Fe–N<sub>4</sub> in acidic media (Fig. 2a). The as-prepared HP-Fe–N<sub>4</sub> showed a higher onset potential ( $E_{\text{onset}}$ , 0.95 V *vs.* the reversible hydrogen electrode, RHE) and a more positive  $E_{1/2}$  (0.80 V) than that of pyridine-type Fe–N<sub>4</sub> (0.86 V and 0.71 V, respectively). DFT calculations demonstrate that the pyrrole-type Fe–N<sub>4</sub> shows stronger electron depletion around the Fe atom than pyridine-type Fe–N<sub>4</sub>, enabling preferred O<sub>2</sub> adsorption energy and complete four-electron reaction selectivity for the ORR. Recently, Jaouen and co-workers systematically investigated the durability and degradation of the Fe–N<sub>4</sub> site by combining *operando* <sup>57</sup>Fe Mössbauer spectroscopy and XAS.<sup>98</sup> They firstly identified two types of Fe–N<sub>4</sub> sites in the Fe–N–C electrocatalyst, including a high-spin FeN<sub>4</sub>C<sub>12</sub> moiety (denoted as S1, pyrrole-type Fe–N<sub>4</sub>) and a low- or intermediate-spin FeN<sub>4</sub>C<sub>10</sub> moiety (denoted as S2, pyridine-type Fe–N<sub>4</sub>). Both FeN<sub>4</sub>C<sub>12</sub> and FeN<sub>4</sub>C<sub>10</sub> sites initially contributed to the ORR activity of Fe–N–C in an acidic medium and the FeN<sub>4</sub>C<sub>12</sub> site was found to be more intrinsically active in the beginning. However, FeN<sub>4</sub>C<sub>12</sub> was not durable in operating PEMFCs, quickly transforming to ferric oxides (Fig. 2b). In contrast, the number of less active FeN<sub>4</sub>C<sub>10</sub> sites remained unchanged after 50 h operation at 0.5 V, maintaining the PEMFC performance after initial



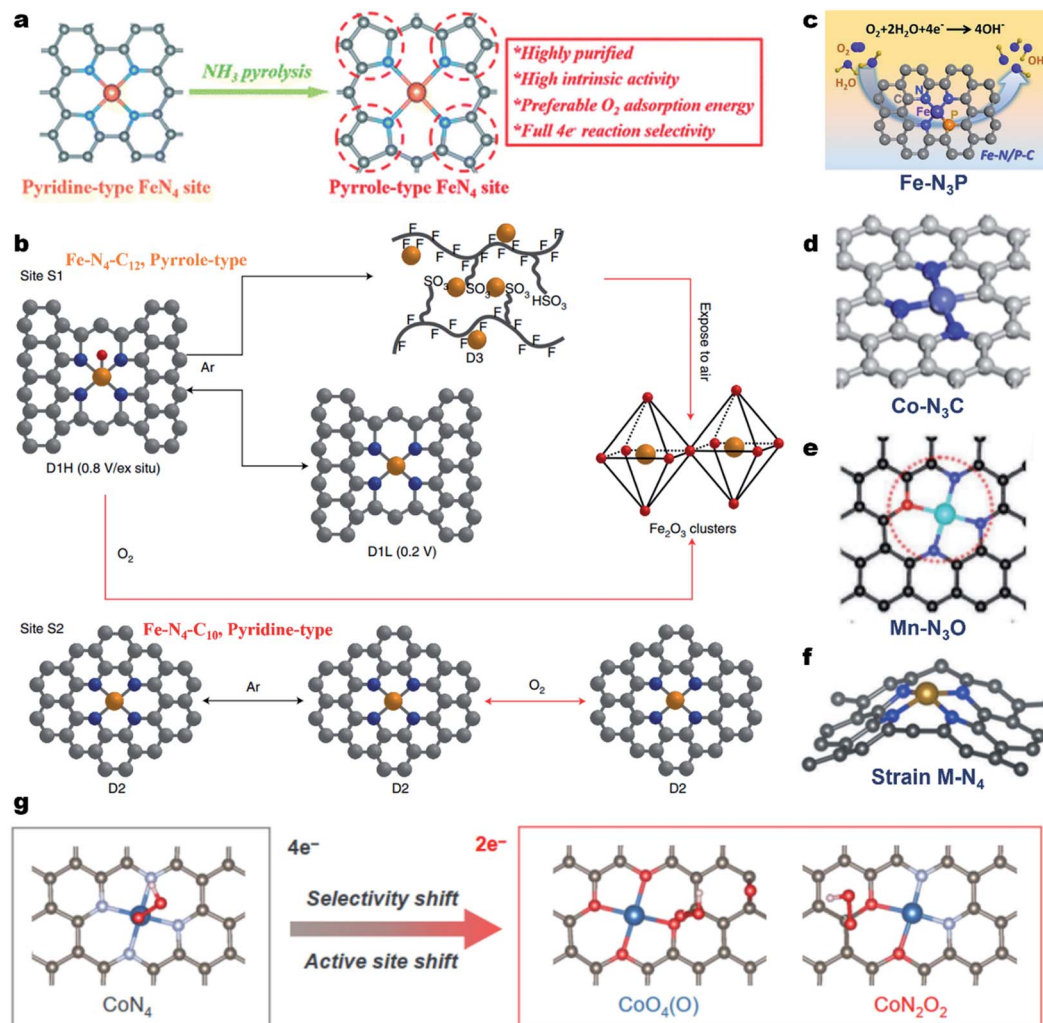


**Fig. 2** Regulation of the coordination geometry of the metal center for enhancing the ORR activity. (a) Preparation process of the high-purity pyrrole-type Fe-N<sub>4</sub> structure. Reproduced with permission from ref. 97. Copyright (2020) Royal Society of Chemistry. (b) Coordination and structural changes of the sites S1 and S2 under *in situ* or *operando* conditions. Reproduced with permission from ref. 98. Copyright (2020) Springer Nature. (c) Schematic showing the N and P co-ordinated single Fe site (Fe-N<sub>3</sub>P). Reproduced with permission from ref. 104. Copyright (2020) American Chemical Society. (d) Schematic showing the N and C co-ordinated single Co site (Co-N<sub>3</sub>C). Reproduced with permission from ref. 106. Copyright (2020) American Chemical Society. (e) Schematic showing the N and O co-ordinated single Mn site (Mn-N<sub>3</sub>O). Reproduced with permission from ref. 109. Copyright (2018) Wiley-VCH. (f) Schematic showing the strained M-N<sub>4</sub> site. Reproduced with permission from ref. 112. Copyright (2019) WILEY-VCH. (g) OOH\* adsorption on CoN<sub>4</sub> and CoO<sub>4</sub>(O), and CoN<sub>2</sub>O<sub>2</sub> sites. Reproduced with permission from ref. 117. Copyright (2021) American Chemical Society.

degradation. This work presented a profound comprehension of the local coordination effect on the ORR activity and a fundamental understanding of the degradation of Fe-N<sub>4</sub> sites. Importantly, it provided a new direction for the rational design of durable Fe-N-C catalysts.

On the other hand, the N atoms in Fe-N<sub>4</sub> could be replaced with other atoms for the formation of the Fe-N<sub>4-x</sub>A<sub>x</sub> geometry (A = C, S, P, B or O), resulting in a modulated electronic structure and tailored ORR properties.<sup>99–103</sup> For example, Yuan *et al.* prepared N/P dual-coordinated Fe sites by pyrolysis of polypyrrole (PPy)/phytic acid/FeCl<sub>3</sub>. The aberration-corrected HAADF-STEM image, XANES and EXAFS investigations proved that the Fe was coordinated with three N atoms and one P atom, forming the Fe-N<sub>3</sub>P<sub>1</sub>. Electrochemical tests and DFT calculations

demonstrated that the Fe-N<sub>3</sub>P<sub>1</sub> sites were more favorable for oxygen intermediate adsorption/desorption, leading to accelerated reaction kinetics and promising ORR activity (Fig. 2c).<sup>104</sup> The local coordination geometry could also affect the catalytic properties of Cu-N-C,<sup>105</sup> Co-N-C,<sup>106–108</sup> Mn-N-C,<sup>109</sup> Mg-N-C,<sup>110</sup> Ni-N-C,<sup>111</sup> and Zn-N-C<sup>58</sup> electrocatalysts. For instance, the ORR tests and DFT calculation results indicated that Co-N<sub>3</sub>C presented the best catalytic activity among Co-N<sub>3</sub>C<sub>1</sub>, Co-N<sub>2</sub>C<sub>2</sub>, and Co-N<sub>4</sub> (Fig. 2d).<sup>106</sup> The N/O dual coordinated Mn-N<sub>x</sub>O<sub>y</sub> active sites exhibited higher ORR activity than that of Mn-N<sub>4</sub> and the Mn-N<sub>3</sub>O<sub>1</sub> configuration displayed the best intrinsic ORR activity among all reported Mn-N<sub>x</sub>O<sub>y</sub> sites (Fig. 2e).<sup>109</sup> Besides, the introduction of the local strain effect around M-N<sub>x</sub> sites could also tailor the ORR performance of M-N-C materials



(Fig. 2f).<sup>112–115</sup> Tailoring the local coordination geometry can also tune the catalytic pathway and selectivity. For instance, Qiao *et al.* synthesized a Mo single atom catalyst with a unique O, S coordination (Mo<sub>1</sub>/OSG-H) that could catalyze the ORR *via* the 2e<sup>-</sup> pathway with a high H<sub>2</sub>O<sub>2</sub> selectivity of >95% in 0.1 M KOH.<sup>116</sup> Apart from first-shell coordination, the second coordination sphere also largely alters the electronic structures of active sites through structural effects and manipulates intermediate adsorption through the space effect, thus changing the catalytic ORR pathway and selectivity. Very recently, the same group constructed a CoNOC catalyst with N, O-dual coordination and C–O–C functional groups that demonstrated outstanding activity and a selectivity of >95% for acidic H<sub>2</sub>O<sub>2</sub> electrosynthesis relative to the CoN<sub>4</sub> site.<sup>117</sup> DFT computations, poisoning experiments, and *in situ* attenuated total reflectance surface-enhanced infrared absorption spectroscopy suggested that an active site (especially for OOH\* adsorption) shifted from the center Co atom to the O-adjacent C atom, enabling a superior 2e<sup>-</sup> ORR pathway (Fig. 2g).

These studies clearly demonstrated that the local coordination geometry will largely affect the catalytic ORR behavior. Precisely engineering the coordination configurations of the single atom site and molecular-level understanding of actual active sites are essential to correlate the structure–performance relationship and pursue advanced M–N–C electrocatalysts, but they remain a huge challenge.

## 2.2 Heteroatom incorporation

Aside from direct coordination with the central atom, a heteroatom (*i.e.*, S, P, B or O) can also be incorporated into the carbon

skeleton.<sup>83,118</sup> Such an incorporated heteroatom with a different atomic size and electronegativity (compared to N and C atoms) can affect the electronic structure of the single M–N<sub>x</sub> sites *via* long-range delocalization.<sup>119–122</sup> In 2015, Sun *et al.* for the first time synthesized a S doped Fe–N–C catalyst and validated the promotional role of S dopant in the ORR.<sup>123</sup> Later on, Li *et al.* demonstrated a volcano relationship between the ORR activity and the S incorporation content.<sup>124</sup> In a 0.1 M KOH solution, the Fe-ISA/SNC catalyst with a N/S atomic ratio of 1/1 achieved the highest ORR activity (Fig. 3a and b) with an  $E_{1/2}$  of 0.896 V (*vs.* RHE). XAS investigation and DFT calculations revealed that the relatively low electronegativity of S could enrich the charge on a N atom, which facilitated the rate-limiting reductive release of OH\* and accelerated the overall ORR process. The influence of S-containing functional groups (*e.g.*, thiophene-S and oxidized-S species) on the ORR activity was further investigated by Lee *et al.*<sup>125</sup> They found that the oxidized S functionality decreased the d-band center of iron by withdrawing electrons, thereby facilitating the ORR at the Fe–N<sub>4</sub> site by lowering the intermediate adsorption energy. In contrast, the thiophene-S structure with electron-donating properties reduced the intrinsic ORR activity of the Fe–N<sub>4</sub> site (Fig. 3c).<sup>126</sup> Beside S, P,<sup>127</sup> B,<sup>128</sup> or co-doping S and P<sup>129</sup> could also induce uneven charge density distribution, hence altering the intrinsic activity of Fe–N<sub>x</sub> sites. In 2018, Wang and co-workers developed a novel MOF@polymer strategy for the construction of single Fe atomic sites supported on a N, P and S co-doped hollow carbon polyhedron (Fe-SAs/NPS-HC).<sup>129</sup> The single Fe atom was coordinated with four N atoms for the formation of Fe–N<sub>4</sub> and the S and P atoms

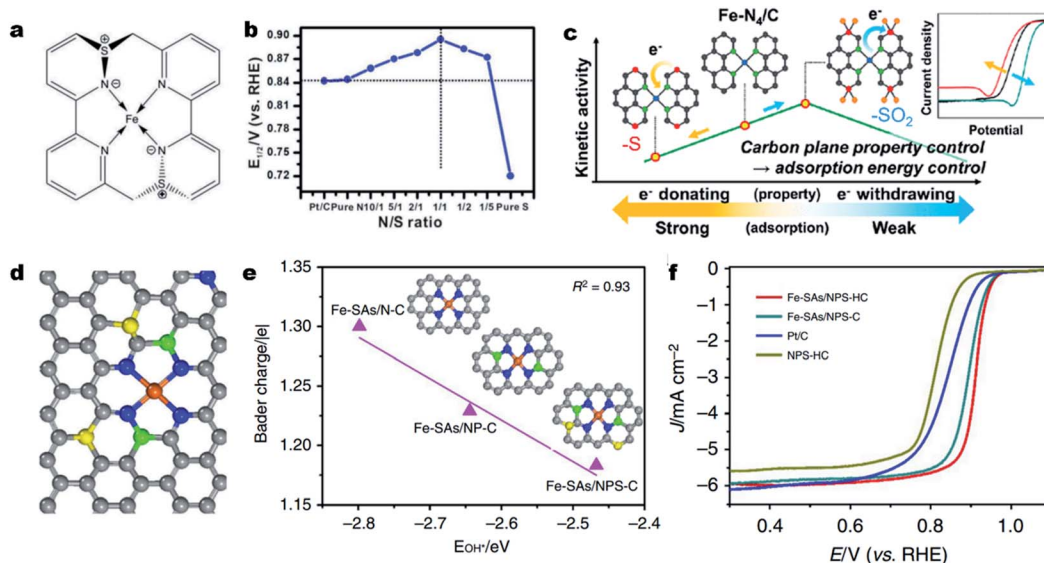


**Fig. 3** Heteroatom incorporation for promoting the ORR activity. (a) Structure of the FeN<sub>4</sub>S<sub>2</sub> active site in Fe-ISA/SNC. (b) Line graph of the relationship between the N/S ratio and corresponding  $E_{1/2}$  of different Fe-ISA/SNC samples, showing that the Fe-ISA/SNC with a N/S ratio of 1/1 presents the highest  $E_{1/2}$ . Reproduced with permission from ref. 124. Copyright (2018) WILEY-VCH. (c) Plot for the kinetic activity of a Fe–N–C catalyst as a function of the electron-donating/withdrawing properties of S dopants. Reproduced with permission from ref. 125. Copyright (2019) American Chemical Society. (d) Schematic model of Fe-SAs/NPS-HC, Fe (orange), N (blue), P (green), S (yellow) and C (gray). (e) Linear relationship between the OH\* binding energy and Bader charge of single-atom iron in Fe-SAs/N–C, Fe-SAs/NP–C and Fe-SAs/NPS–C, respectively. Insets: the corresponding schematic models of samples, Fe (orange), N (blue), P (green), S (yellow) and C (gray). (f) ORR polarization curves for Fe-SAs/NPS-HC, Fe-SAs/NPS-C, NPS-HC and 20% Pt/C. Reproduced with permission from ref. 129. Copyright (2021) Springer Nature.



were doped into the carbon skeleton (Fig. 3d). DFT calculations indicate that the surrounding S and P atoms can donate electrons to the single-atom Fe center, making the charge of Fe ( $\text{Fe}^{\delta+}$ ) less positive and weakening the binding of adsorbed OH species (Fig. 3e). As a result, the as-prepared Fe-SAs/NPS-HC demonstrated superior ORR activity in both alkaline and acidic solutions, achieving a high  $E_{1/2}$  of 0.912 V and 0.791 V (vs. RHE), respectively (Fig. 3f). Moreover, the above dopants could as well regulate the electronic structure and improve the intrinsic activity of single  $\text{Co-N}_x$ ,<sup>130</sup>  $\text{Cu-N}_x$ ,<sup>59</sup> and  $\text{Mn-N}_x$ .<sup>131,132</sup> sites for  $\text{Co-N-C}$ ,  $\text{Cu-N-C}$  and  $\text{Mn-N-C}$  electrocatalysts, respectively.

### 2.3 Axial ligand modification

It is noted that the d orbitals of the single metal sites perpendicular to the  $\text{M-N-C}$  plane are not fully occupied and can

potentially interact with small ligands (*e.g.*, small molecules, or anions). Such ligands can coordinate with the single metal atoms and modulate the electronic structure of the  $\text{M-N}_x$ .<sup>133–136</sup> Cho *et al.* first designed a penta-coordinated  $\text{FePc-Py-CNT}$  catalyst by immobilizing  $\text{FePc}$  molecules on pyridine-functionalized carbon nanotubes (CNTs) (Fig. 4a).<sup>137</sup> Thanks to the synergy of the penta-coordinated structure and CNTs for efficient electron transfer, the synthesized  $\text{FePc-Py-CNTs}$  exhibited good ORR activity in alkaline solutions, better than that of  $\text{Pt/C}$ . Such a promotional role of axial ligands could also be found in Fe porphyrins. The creation of strong axial coordination can further enhance the ORR activity and stability of  $\text{FePc}$ . As shown in Fig. 4b,  $\text{FePc}$  could coordinate with oxygen-containing groups on an  $\text{O}_2$  plasma-treated acetylene black (AB-O) matrix, forming an  $\text{FeAB-O}$  catalyst. For comparison,  $\text{FePc/AB}$  was prepared by physically mixing  $\text{FePc}$  and AB. DFT

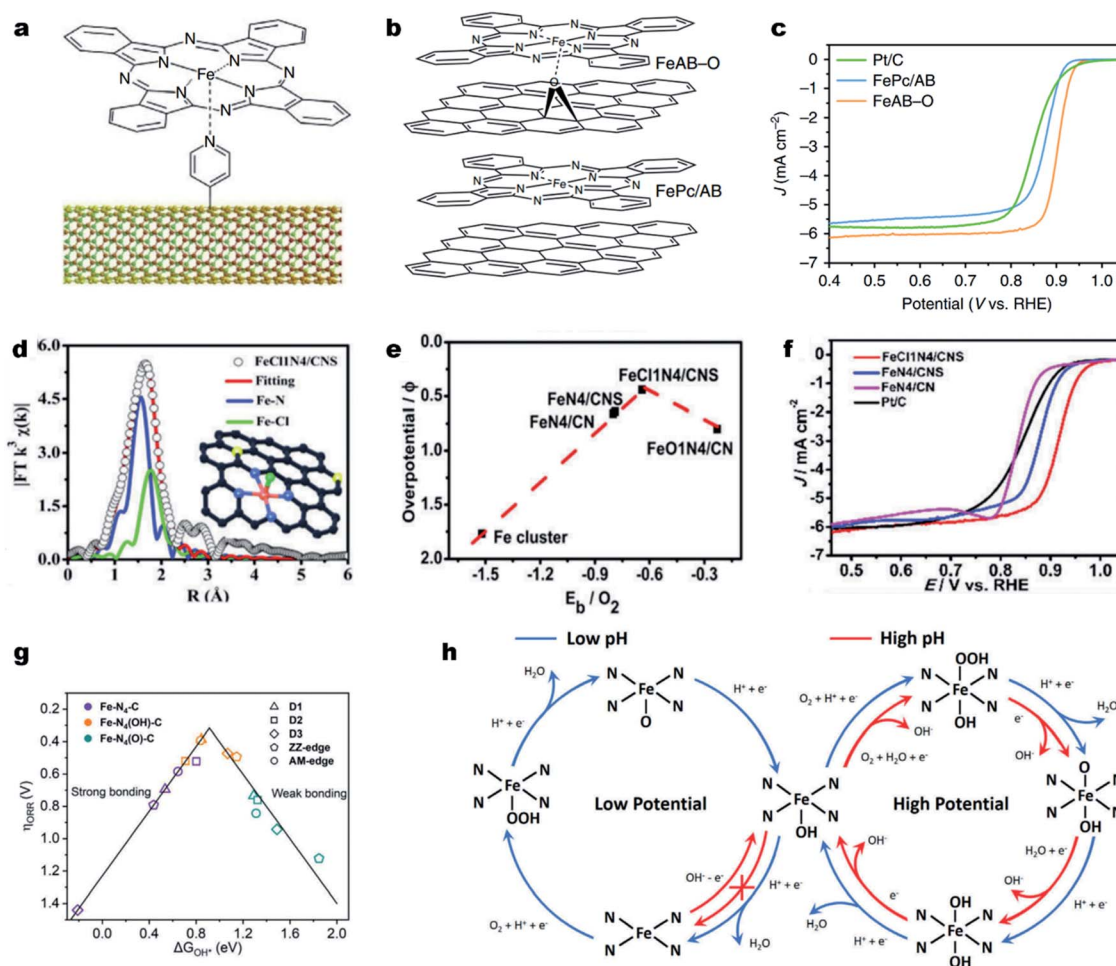


Fig. 4 Engineering axial ligands on  $\text{Fe-N}_x$  for improving the ORR activity. (a) Schematic diagram of the structure of the  $\text{FePc-Py-CNT}$  composite. Reproduced with permission from ref. 137. Copyright (2013) Springer Nature. (b) Molecular structure models of  $\text{FeAB-O}$  and  $\text{FePc/AB}$ . (c) ORR polarization curves of  $\text{FeAB-O}$ ,  $\text{FePc/AB}$ , and  $\text{Pt/C}$  in  $\text{O}_2$ -saturated 0.1 M  $\text{KOH}$ . Reproduced with permission from ref. 143. Copyright (2020) Springer Nature. (d) EXAFS fitting curves of the  $\text{FeCl}_1\text{N}_4/\text{CNS}$  in the  $R$  space. Inset: Schematic model of  $\text{FeCl}_1\text{N}_4/\text{CNS}$ : Fe (red), Cl (green), S (yellow), N (blue), and C (gray). (e) The correlation of the ORR overpotentials with the  $\text{O}_2$  binding energies for the Fe catalysts. (f) ORR polarization curves of different catalysts in  $\text{O}_2$ -saturated 0.1 M  $\text{KOH}$ . Reproduced with permission from ref. 138. Copyright (2018) Royal Society of Chemistry. (g) Volcano plot between  $\Delta G^*_{\text{OH}}$  and the ORR overpotential for five  $\text{Fe-N}_4\text{-C}$  structures with different axial ligands. (h) Schematic illustration of reaction pathways for the ORR on  $\text{Fe-N}_4$  moieties in acidic and alkaline solutions under ORR working potentials. Reproduced with permission from ref. 142. Copyright (2020) WILEY-VCH.



calculations imply that the axial O coordination (O-FeN<sub>4</sub>) sites can greatly break the electronic distribution symmetry of Fe and lead to electron localization on O. This electron localization strengthened O<sub>2</sub> adsorption and accelerated charge transfer from the Fe to the O<sub>2</sub> molecule. As a result, the FeAB-O catalyst exhibited fast ORR kinetics with a remarkable  $E_{1/2}$  of 0.90 V (vs. RHE), which was much higher than those of FePc/AB (0.87 V) and Pt/C (0.85 V) (Fig. 4c).

Halogen ions, such as chloride ions (Cl<sup>-</sup>), displayed strong coordination ability with transition metal atoms. For example, Han *et al.* modified pristine Fe-N<sub>4</sub> active sites with axial Cl coordination for the formation of Fe-Cl<sub>1</sub>N<sub>4</sub> sites decorated on the N, S co-doped carbon (FeCl<sub>1</sub>N<sub>4</sub>/CNS) (Fig. 4d).<sup>138</sup> Due to the synergistic effect of the Cl ligand and S dopant, FeCl<sub>1</sub>N<sub>4</sub>/CNS exhibited a much lower overpotential (0.44 V) than that of FeN<sub>4</sub>/CN (0.66 V) and possessed a moderate binding energy of O<sub>2</sub> ( $E_b$  = 0.64 eV) (Fig. 4e), indicating a favorable ORR activity. In 0.1 M KOH, FeCl<sub>1</sub>N<sub>4</sub>/CNS displayed an unexpectedly excellent ORR activity with an  $E_{1/2}$  of 0.921 V (vs. RHE) (Fig. 4f).

Recent investigations also revealed a self-adjusting mechanism induced by its intrinsic intermediate (such as \*OH) during the ORR process for enhancing the intrinsic activity of M-N-C materials.<sup>46,139,140</sup> Using DFT simulations, Zhou and co-workers found that the single Fe site of Fe-N-C was preferentially covered with an intrinsic intermediate OH\* from 0.28 to 1.00 V (vs. RHE). Such OH\* became part of the Fe center for the formation of Fe(OH)N<sub>4</sub> and optimized the intermediate binding, promoting the ORR kinetics.<sup>141</sup> Li *et al.* also investigated the self-adjusting mechanism on different Fe-N<sub>4</sub> configurations, including Fe-N<sub>4</sub>-C<sub>10</sub> (D1), Fe-N<sub>4</sub>-C<sub>12</sub> (D2), Fe-N<sub>4</sub>-C<sub>8</sub> (D3), zigzag edge Fe-N<sub>4</sub>-C (ZZ-edge) and armchair edge Fe-N<sub>4</sub>-C (AM-edge) and obtained the same conclusions (Fig. 4g).<sup>142</sup> The axial OH ligand could be formed under certain electrode potentials as an intermediate during the ORR or directly from the alkaline solution (Fig. 4h). Remarkably, the OH ligand decreased the bonding strength of ORR intermediates on a single Fe site and therefore accelerated the catalytic activity of Fe-N<sub>4</sub> moieties. The profound understanding of the promotional effect of the axial ligand on the ORR activity on Fe-N-C electrocatalysts motivates the design of highly active and stable Fe-N<sub>x</sub> sites, such as higher coordination configurations, Fe-N<sub>5</sub> and Fe-N<sub>6</sub>.

## 2.4 Dual metal sites

The adjacent M-N<sub>x</sub> sites can hardly influence each other's electronic structure and intrinsic activity if they are far apart in the carbon substrate.<sup>144</sup> When the distance goes to several angstroms, the electronic structures of M-N<sub>x</sub> and M'-N<sub>x</sub> may affect each other.<sup>145,146</sup> Yu *et al.* demonstrated strong electronic interactions between the adjacent Fe-N<sub>4</sub> sites over the Fe-N-C material when the inter-site distance ( $d_{\text{site}}$ ) was less than about 1.6 nm (Fig. 5a).<sup>147</sup> When the  $d_{\text{site}}$  was about 0.7 nm, the Fe-N<sub>4</sub> showed much enhanced ORR intrinsic activity (Fig. 5b). Fu *et al.* constructed a single-atom dispersed Zn/Cu-NC catalyst with Zn-N<sub>4</sub> together with Cu-N<sub>4</sub> and proposed that the adjacent Zn sites could modify the d-orbital electron configuration of Cu-N<sub>4</sub>

sites.<sup>148</sup> The modified Cu-N<sub>4</sub> catalytically active site could facilitate the O-O bond breakage and reduce the energy barrier for OOH\* conversion, thus promoting the ORR activity. The synergistic effect could also be observed on (Fe,Co)-SA/CS, where the Fe modulated single atom Co-N<sub>4</sub> acted as the strengthened active site.<sup>149</sup>

Further decreasing the distance, the M and M' could coordinate with each other and form the "real" closest dual metal sites, *i.e.*, M-M'-N<sub>x</sub> (Fig. 5c).<sup>150,151</sup> The M and M' can largely alter each other's electronic structure through metal-metal interactions and charge polarization,<sup>152,153</sup> therefore changing the O<sub>2</sub> adsorption behavior, and the subsequent ORR pathway. For example, Wang *et al.* used a double-solvent method for the construction of an Fe-Co dual-site (Fe,Co)/N-C catalyst and achieved superior ORR activity in acidic media to those of single Co or Fe site.<sup>154</sup> The HAADF-STEM image and Mössbauer spectroscopy indicated the presence of Co-Fe dual sites. The DFT calculations suggest that the Fe-Co dual-site could reduce the energy barrier of OOH\* dissociation into O\* and OH\*, enabling a faster ORR kinetics. Further, an OH-ligand self-binding approach was discovered to enhance the Fe-Co dual-site.<sup>151</sup> The pristine binuclear FeCoN<sub>5</sub> site promoted a bridging-*cis* O<sub>2</sub> adsorption configuration, making the O-O bond easier to cleave (Fig. 5d). In the ORR process, the *in situ* generated FeCoN<sub>5</sub>-OH site decreased the localized electron density around single Fe atoms, leading to a weakened Fe-O bonding and dramatically improved intrinsic ORR activity. As a result, the as-constructed FeCoN<sub>5</sub>-OH site delivered an ORR  $E_{\text{onset}}$  and  $E_{1/2}$  of up to 1.02 and 0.86 V (vs. RHE), respectively, with an intrinsic activity over 20 times higher than that of the single-atom Fe-N<sub>4</sub> site in a 0.1 M HClO<sub>4</sub> electrolyte solution (Fig. 5e). Besides, the Mn-N<sub>4</sub> site can also change the spin state of the neighboring Fe-N<sub>4</sub> site from the low spin state ( $t_{2g}^5e_g^0$ ) to the intermediate spin state ( $t_{2g}^4e_g^1$ ) (Fig. 5f). The magnetic susceptibility results indicated that the effective magnetic moment of Fe,Mn/N-C and Fe/N-C was 3.75  $\mu_{\text{eff}}$  and 2.16  $\mu_{\text{eff}}$ , respectively (Fig. 5g and h).<sup>155</sup> DFT calculations reveal that the tailored Fe,Mn/N-C catalyst can interact with oxygen moderately, with appropriate bond length and adsorption energy, beneficial to promote the ORR kinetics. As a result, the Fe,Mn/N-C catalyst displayed excellent ORR activity in both 0.1 M HClO<sub>4</sub> and 0.1 M KOH solutions with a high  $E_{1/2}$  of 0.804 and 0.928 V (vs. RHE), respectively.

Besides, a dual metal sites can be constructed using an identical metal species for the formation of M<sub>2</sub>-N-C as well.<sup>156</sup> Xiong *et al.* prepared single site Fe<sub>1</sub>-N-C, dual site Fe<sub>2</sub>-N-C, and triple site Fe<sub>3</sub>-N-C by pyrolysis of specific Fe atoms as precursors encapsulated in a zeolitic imidazolate framework (ZIF-8).<sup>157</sup> The dual site Fe<sub>2</sub>-N-C prepared from the binuclear Fe<sub>2</sub>(-CO)<sub>9</sub>@ZIF-8 hybrid structure displayed excellent ORR activity and durability in an acidic solution, which was superior to those of Fe<sub>1</sub>-N-C and Fe<sub>3</sub>-N-C. They found that the dual site Fe<sub>2</sub> cluster in Fe<sub>2</sub>-N-C and the triple site Fe<sub>3</sub> cluster in Fe<sub>3</sub>-N-C adsorbed the O<sub>2</sub> in a side-on configuration, enabling better O<sub>2</sub> activation than Fe-N-C. However, Fe<sub>2</sub>-N-C had more catalytic sites and more enhanced bonding hybridization between Fe 3d and O 2p orbitals than Fe<sub>3</sub>-N-C, making Fe<sub>2</sub>-N-C more active. A



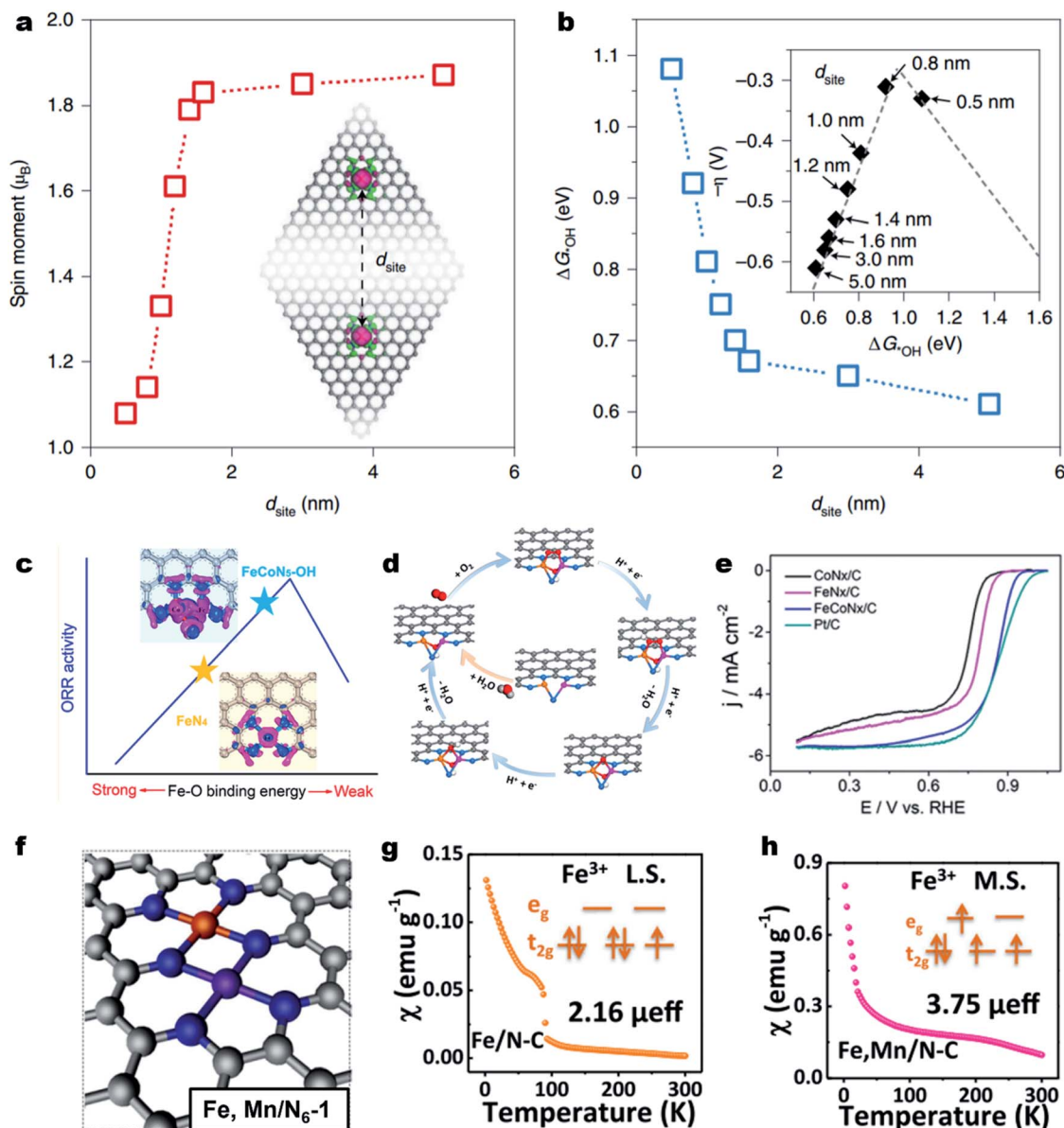


Fig. 5 Survey of the dual metal sites for enhancing the ORR activity. (a) DFT calculated on-site magnetic moments of Fe atoms interacting with neighboring sites with different  $d_{\text{site}}$  values. (b) The  $d_{\text{site}}$ -dependent  $\Delta G_{\text{OH}}^*$  obtained by DFT calculations. Inset: volcano plot of calculated overpotentials for the ORR against  $\Delta G_{\text{OH}}^*$ . Reproduced with permission from ref. 147. Copyright (2021) Springer Nature. (c) Improving the intrinsic activity of Fe- $N_4$  site by Co-Fe dual site construction. (d) Proposed ORR mechanism on the FeCo $N_5$ -OH site. (e) ORR polarization curves of Co $N_x$ /C, Fe $N_x$ /C, FeCo $N_x$ -C and Pt/C in a 0.1 M HClO $_4$  solution. Reproduced with permission from ref. 151. Copyright (2019) American Chemical Society. (f) Optimized structure of Fe, Mn/N $_6$ -1. Magnetic susceptibility of (g) Fe/N-C and (h) Fe, Mn/N-C (M.S. represents medium-spin and L.S. represents low-spin). Reproduced with permission from ref. 155. Copyright (2021) Springer Nature.

similar phenomenon was reported by Xie *et al.*, where the Fe $_2$ N $_6$  site was more active than Fe- $N_4$ .<sup>158</sup> These results discussed above provide new insights into the design of dual metal sites and the fundamental understanding of the ORR mechanism at the atomic level.

### 2.5 Regulation of the carbon skeleton geometry

The geometric configuration of the carbon skeleton can also largely alter the electronic structure of M- $N_x$  sites, thus regulating the intrinsic ORR activity.<sup>159</sup> For example, the Fe- $N_4$

active moiety can exist in different forms, such as micropore-hosted Fe- $N_4$ -C $_8$ , Fe- $N_4$ -C $_{10}$  and Fe- $N_4$ -C $_{12}$ , depending on the surrounding carbon geometry (Fig. 6a).<sup>160</sup> Their ORR properties were theoretically investigated. As illustrated in Fig. 6b, the O $_2$  was adsorbed on Fe- $N_4$ -C $_8$  in a side-on configuration, while it was adsorbed on Fe- $N_4$ -C $_{10}$  and Fe- $N_4$ -C $_{12}$  in an end-on configuration (Fig. 6b). As a result, Fe- $N_4$ -C $_8$  has the lowest activation energy for O $_2$  and OOH dissociation and favors a direct four-electron pathway (Fig. 6c). Using advanced  $^{57}\text{Fe}$  Mössbauer spectroscopy, Wu *et al.* identified Fe- $N_4$ -C $_8$  and Fe-





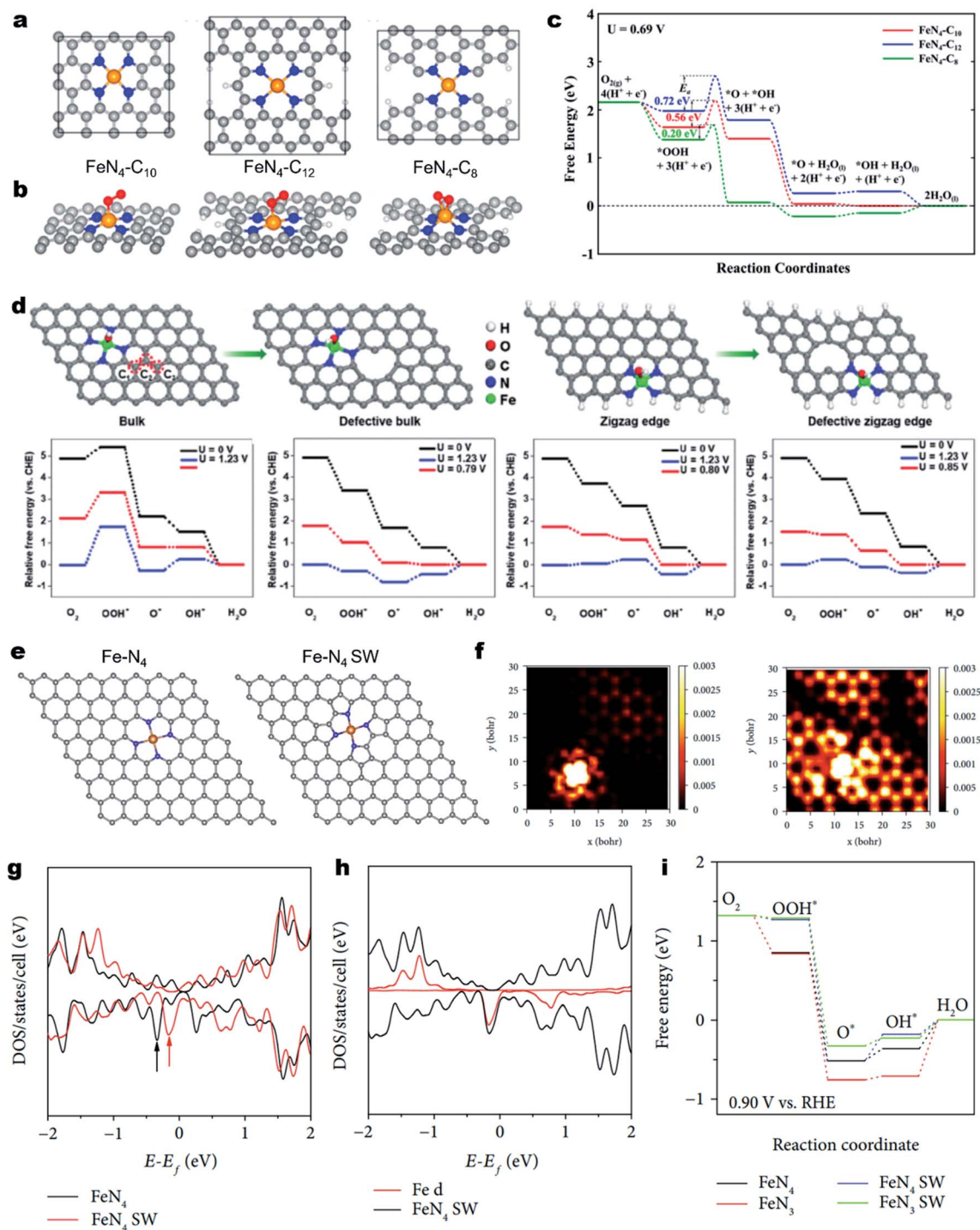


**Fig. 6** Regulating the carbon skeleton geometry for enhancing the ORR activity. (a) Atomistic configuration of the Fe–N<sub>4</sub> moiety with different local carbon structures of Fe–N<sub>4</sub>–C<sub>10</sub>, Fe–N<sub>4</sub>–C<sub>12</sub>, and Fe–N<sub>4</sub>–C<sub>8</sub> and (b) corresponding O<sub>2</sub> adsorption configuration. (c) Calculated free energy diagrams for the ORR through an OOH dissociation pathway on the above three different active sites under a potential of 0.69 V in acidic medium. Reproduced with permission from ref. 160. Copyright (2017) American Chemical Society. (d) Schematic illustration of a bulk Fe–N<sub>4</sub> site, defective bulk Fe–N<sub>4</sub> site, zigzag Fe–N<sub>4</sub> site, and defective zigzag Fe–N<sub>4</sub> site and corresponding free energy diagram for the ORR. Reproduced with permission from ref. 163. Copyright (2019) Wiley-VCH. (e) Atomic models of Fe–N<sub>4</sub> and Fe–N<sub>4</sub> SW. (f) Simulated STM image (at a bias of –1.0 V) of normal Fe–N<sub>4</sub> doped graphene sheets (left) and Fe–N<sub>4</sub> SW doped graphene sheets (right). Density of states (DOS) of normal Fe–N<sub>4</sub> and Fe–N<sub>4</sub> SW-doped graphene sheets. (g) DOS of Fe–N<sub>4</sub> SW and (h) DOS of Fe 3d. (i) Free energy diagrams of ORR processes on normal Fe–N<sub>4</sub>, normal Fe–N<sub>3</sub>, Fe–N<sub>4</sub> SW, and Fe–N<sub>3</sub> SW at the applied potential of +0.9 V vs. RHE. Reproduced with permission from ref. 165. Copyright (2019) the American Association for the Advancement of Science.



$N_4-C_{10}$  in an atomically dispersed Fe–N–C catalyst and experimentally found that Fe– $N_4-C_8$  was more active for the ORR.<sup>161</sup> Due to the rich Fe– $N_4-C_8$  site, the as-developed Fe–N–C demonstrated excellent ORR activity with a high  $E_{1/2}$  of 0.88 V (vs. RHE) in 0.5 M  $H_2SO_4$ , which was comparable to that of Pt/C.

Besides, carbon defects can also induce redistribution of the charge density of the single metal atoms and the neighboring N atoms. In 2017, Zelenay *et al.* firstly proposed that Fe– $N_4$  moieties at the edges of graphitic domains might have higher ORR activity.<sup>46</sup> Later on, Yao *et al.* demonstrated the local electronic redistribution and bandgap shrinkage of the edge-Fe– $N_4$  site, enabling a lower free-energy barrier toward the direct four-electron ORR.<sup>162</sup> The utilization of  $NH_4Cl$  salt was found to be a promising approach for the creation of abundant edge-Fe– $N_4$  sites.<sup>163</sup>  $NH_4Cl$  enabled the preferential formation of edge-Fe– $N_4$  sites and favored the formation of numerous pores and N-doped edges. DFT calculations confirm that the introduced in-plane holes could lower the adsorption energy of intermediates (*e.g.*,  $O_2^*$  and  $OOH^*$ ), thereby promoting the intrinsic ORR activity (Fig. 6d). Subsequently, the edge-Fe– $N_4$  site anchored Fe $N_x$ /GM catalysts demonstrated remarkable ORR activity in acid media. Moreover, the PEMFC using Fe $N_x$ /GM as the cathode catalyst exhibited an impressive maximum power density ( $P_{max}$ ) value of 0.43 W  $cm^{-2}$  under air conditions.

In addition, the topological defect is another regulatory factor of M– $N_x$  site's intrinsic activity of the M– $N_x$  site. Using DFT calculations, Yang *et al.* revealed that the defective graphene skeleton with pentagon–octagon–pentagon (585) defects could efficiently mediate charge redistribution of the attached exfoliated monolayer iron phthalocyanine (FePc), providing the FePc with enhanced ORR activity.<sup>164</sup> Moreover, the Fe– $N_4$  in the Stone–Wales (SW) defect (pentagon–heptagon–heptagon–pentagon, 5775 defects) configurations also displayed enhanced catalytic performance relative to the pristine Fe– $N_4$  (Fig. 6e).<sup>165</sup> As depicted in Fig. 6f, the simulated scanning tunneling microscopy (STM) images demonstrated that the SW defects caused significant redistribution of electron densities of Fe– $N_4$  and adjacent carbon atoms. Fig. 6g and h show the total density of states (DOS) of normal and SW Fe–N centers. Notably, the marked state of Fe– $N_4$  SW is much closer to the Fermi level than that of normal Fe– $N_4$ , indicating higher ability for donating electrons and reducing oxygen. The ORR free energy diagrams further add the evidence that the Fe– $N_4$  SW has a lower reaction overpotential than the normal counterpart (Fig. 6i).<sup>165</sup> In contrast, the neighboring SW defect or 585 defects would lower the intrinsic ORR activity of the M– $N_x$  sites.<sup>166</sup>

These studies highlight the essential role of carbon defects and inspire the rational design of more advanced Fe–N–C catalysts for the ORR *via* such a pore/edge/topological-engineering strategy. Similar to Fe–N–C materials, engineering of the local carbon structure of Co– $N_x$  and Mn– $N_x$  sites can also enhance their corresponding intrinsic ORR activities.<sup>167,168</sup> Although several investigations by theoretical studies have demonstrated the promotional role of the defects in the ORR, further efforts regarding the precise identification of the edge or topological defects are indispensable, requiring accurate atomic TEM scrutinization.

### 3. Engineering dense active sites

Aside from improving the intrinsic ORR activity of the M– $N_x$  active site as discussed above, it is essential to maximize the density of active sites over single atom carbonous M–N–C electrocatalysts for enhancing the ORR activity.<sup>169</sup> However, currently reported strategies for synthesizing M–N–C materials unavoidably involve high-temperature pyrolysis of metal- and N-containing precursors. Unfortunately, during the thermal pyrolysis, metal species tend to agglomerate and eventually form low-active metal-based clusters and nanoparticles (NPs) encapsulated in carbon shells (*e.g.*, M@C NPs). The M@C NPs are typically difficult to remove and thus seriously block the formation of active Fe– $N_x$  moieties, leading to a low density of M– $N_x$  active sites (less than 3.0 at%).

In order to achieve highly active M–N–C electrocatalysts, it is important to prevent the migration and agglomeration of metal atoms during the high-temperature pyrolysis process.<sup>170</sup> Thus, confining the metal atoms within a certain spatial region to prevent their migration becomes one of the effective approaches. The organic/inorganic hybrid frameworks, especially MOFs, with metal–N coordination can adequately prevent the migration of metal atoms.<sup>171</sup> Among the various MOF materials, zeolitic imidazolate frameworks (ZIFs) (*e.g.*, ZIF-8 and ZIF-67) are the most common precursors used due to their easy preparation, and well-defined metal– $N_4$  configurations.<sup>167,172–177</sup> For the synthesis of Fe–N–C electrocatalysts, Fe-doped ZIF-8 can be transformed into Fe single atoms with Zn species being removed due to their lower boiling point ( $\sim 907^\circ C$ ), resulting in atomically dispersed Fe atoms that are confined in ZIF-derived N-doped carbons.<sup>178</sup> Moreover, the Zn vaporization could generate rich micropores, which could host more Fe– $N_4$  active sites.<sup>179–181</sup> For example, Wu *et al.* synthesized an Fe-doped ZIF-8 in an oxygen-free environment and directly converted it into an atomically dispersed Fe–N–C electrocatalyst (Fig. 7a).<sup>182</sup> In the Fe-doped ZIF-8, the Fe– $N_4$  coordination was atomically dispersed and separated by abundant zinc nodes. The special space isolation effect enabled the pyrolyzed Fe–N–C electrocatalyst without Fe aggregation. The particle size of atomic Fe–N–C could be controlled from 20 to 1000 nm by simply adjusting the solution concentration during the synthesis of Fe-doped ZIF-8. Remarkably, the Fe–N–C electrocatalyst with an average particle size of  $\sim 50$  nm displayed the best ORR activity in 0.5 M  $H_2SO_4$  electrolyte with an  $E_{1/2}$  of 0.85 V (vs. RHE), which was only 30 mV lower than that of the Pt/C catalyst. Apart from chemical doping of Fe ions into ZIF-8 precursors, a spatial confinement strategy was also found effective for the synthesis of Fe–N–C electrocatalysts. Li *et al.* developed a novel cage encapsulation strategy to synthesize an atomically dispersed Fe–N–C electrocatalyst (Fig. 7b).<sup>183</sup> ZIF-8 with a cavity diameter of 11.6 Å as molecular cages was employed to encapsulate and separate the iron precursor Fe(acac)<sub>3</sub> (diameter, *ca.* 9.7 nm). During the pyrolysis in an inert atmosphere, isolated single Fe atoms with a high content of 2.16 wt% were stabilized on N doped carbons. In a 0.1 M KOH electrolyte solution, the obtained FeISAs/CN electrocatalyst displayed an excellent ORR



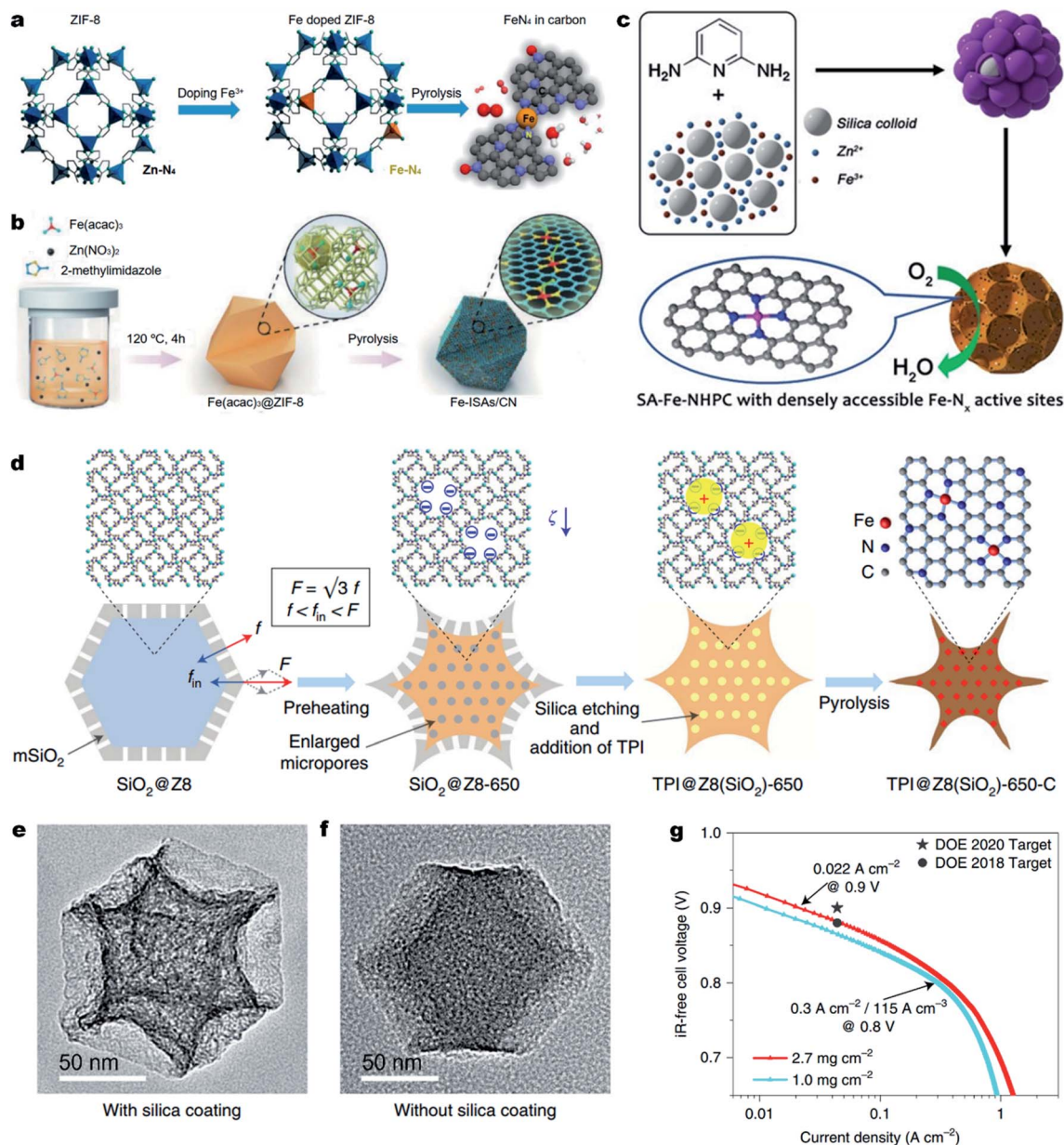


Fig. 7 Engineering dense Fe–N<sub>x</sub> active sites on hierarchically porous carbons. (a and b) One step synthesis of the Fe–N–C electrocatalyst. (a) Space isolation strategy by chemical doping of Fe into ZIF-8 nanocrystals. Reproduced with the permission from ref. 182. Copyright (2017) American Chemical Society. (b) Space confinement by encapsulation of Fe species into the ZIF-8 cavities. Reproduced with the permission from ref. 183. Copyright (2017) Wiley-VCH. (c–g) Enhancing the Fe–N<sub>x</sub> site density and ORR activity by constructing hierarchically porous carbons. (c) Schematic showing the zinc mediated templated synthesis of Fe–N–C with densely accessible Fe–N<sub>x</sub> sites. Reproduced with the permission from ref. 204. Copyright (2020) Wiley-VCH. (d) A schematic synthesis process of TPI@Z8(SiO<sub>2</sub>)-650-C by a mesoporous silica coating strategy. TEM images (e) TPI@Z8(SiO<sub>2</sub>)-650-C and (f) TPI@Z8-650-C. (g) Tafel plot for the determination of the PEMFC performance for TPI@Z8(SiO<sub>2</sub>)-650-C at 0.9 V<sub>iR-free</sub> measured under 1.0 bar H<sub>2</sub>–O<sub>2</sub>. Reproduced with the permission from ref. 205. Copyright (2019) Springer Nature.

performance with an  $E_{1/2}$  of 0.90 V (vs. RHE). Similarly, ferrocene<sup>184</sup> or FePc<sup>185</sup> molecules could also be encapsulated in ZIF-8 for the preparation of atomically dispersed Fe–N–C electrocatalysts. Also, the short-range order nitrogen doped carbon can provide plentiful anchoring sites for the stabilization of single metal sites with strong interaction, enabling the synthesis of high-metal-loading M–N–C electrocatalysts.<sup>186–188</sup>

Previous studies have shown that the surface area and the porosity of M–N–C electrocatalysts play an important role in

ORR performance. A high Brunauer–Emmett–Teller (BET) surface area is beneficial for the ORR catalytic process. The micropores can accommodate abundant M–N<sub>x</sub> active sites and the meso-/macro-pores can facilitate the mass transport. Thus, construction of hierarchically porous carbon nanostructures with a high surface area is an effective strategy to improve the utilization of M–N<sub>x</sub> sites, thus promoting the ORR activity.<sup>189–198</sup> Template sacrificial strategies including a hard template and soft template are common methods to create hierarchically



porous M–N–C electrocatalysts. The template utilizes  $\text{SiO}_2$ ,<sup>74,199–201</sup> SBA-15,<sup>202</sup> molten salts,<sup>169</sup> or Te nanowires<sup>203</sup> as sacrificial templates and small organic molecules, metal complexes or polymers as carbon/nitrogen precursors. In 2020, our group reported the synthesis of densely accessible single atom Fe–N<sub>x</sub> active sites on nitrogen doped hierarchically porous carbon (SA-Fe–NHPC) by a zinc mediated template synthesis strategy.<sup>204</sup> As depicted in Fig. 7c, during the thermal treatment of a N rich 2,6-diaminopyridine/ZnFe/SiO<sub>2</sub> complex, the zinc prevented the formation of Fe<sub>3</sub>C@C nanoparticles and promoted the generation of micropores. In addition, the SiO<sub>2</sub> spheres (~12 nm) served as hard templates for the generation of a mesoporous carbon nanostructure, achieving densely accessible Fe–N<sub>x</sub> active sites on SA-Fe–NHPC. As a result, SA-Fe–NHPC showed a very large specific surface area of 1327 m<sup>2</sup> g<sup>−1</sup> and a high Fe content of 1.25 wt%. Benefiting from the high density and superior accessibility of the Fe–N<sub>x</sub> active sites, the SA-Fe–NHPC electrocatalyst demonstrated high ORR activity with an  $E_{1/2}$  of 0.93 V (vs. RHE) in a 0.1 M KOH aqueous solution. The assembled Zn–air battery using the SA-Fe–NHPC electrocatalyst as an air electrode showed a very high maximum power density ( $P_{\text{max}}$ ) of 266.4 mW cm<sup>−2</sup> and excellent stability for 10 days. Shui *et al.* fabricated a cave-shaped Fe–N–C electrocatalyst (TPI@Z8(SiO<sub>2</sub>)-650-C) with rich meso-porosity, external surface area and dense Fe–N<sub>4</sub> moieties by pyrolyzing mesoporous silica-coated ZIF-8 (Fig. 7d).<sup>205</sup> TPI@Z8-650-C was also synthesized for comparison without the coating of mesoporous SiO<sub>2</sub>. The resultant TPI@Z8(SiO<sub>2</sub>)-650-C exhibited

a large number of mesopores across its surface which presented a three-fold higher external surface area than that of TPI@Z8-650-C (Fig. 7e and f). As a result, the porous TPI@Z8(SiO<sub>2</sub>)-650-C showed much improved ORR activity compared to that of TPI@Z8-650-C in acids. Under the department of energy (DOE) of USA testing protocol, the TPI@Z8-650-C based PEMFC (loading amount: 2.7 mg cm<sup>−2</sup>) achieved a current density of 0.022 A cm<sup>−2</sup> at 0.9 V<sub>iR-free</sub> under 1.0 bar H<sub>2</sub>–O<sub>2</sub> conditions (Fig. 7g). Meanwhile, this TPI@Z8-650-C based PEMFC delivered a  $P_{\text{max}}$  of 1.18 W cm<sup>−2</sup> under 2.5 bar H<sub>2</sub>–O<sub>2</sub>, which approached that of the Pt/C based PEMFC ( $P_{\text{max}} \approx 1.30$  W cm<sup>−2</sup>, loading amount: 0.2 mg<sub>Pt</sub> cm<sup>−2</sup>).

Besides, engineering M–N<sub>x</sub> sites on the surface of carbons will undoubtedly largely improve site utilization. Very recently, Jia *et al.* implemented a chemical vapor deposition (CVD) synthesis, flowing FeCl<sub>3</sub> vapor over a Zn–N–C substrate at 750 °C to prepare accessible Fe–N<sub>4</sub> sites on the surface of carbons (denoted as FeNC-CVD-750) (Fig. 8a).<sup>206</sup> <sup>57</sup>Fe Mössbauer spectroscopy, atomic-resolution annular dark-field STEM (ADF-STEM) and XAS showed the atomically dispersed Fe–N<sub>4</sub> site in the FeNC-CVD-750 catalyst. The number of accessible Fe–N<sub>4</sub> sites (site density,  $SD_{\text{mass}}$ ) was determined by the electrochemical stripping of NO formed by exposure to aqueous nitrite (Fig. 8 and c), and by exposure to gaseous NO (Fig. 3c), giving a  $SD_{\text{mass}}$  value as high as  $1.92 \times 10^{20}$  sites g<sup>−1</sup>. According to the inductively coupled plasma-mass spectrometry (ICP-MS) and <sup>57</sup>Fe Mössbauer spectroscopy, all the Fe–N<sub>4</sub> sites were gas-phase and electrochemically accessible, delivering an Fe site

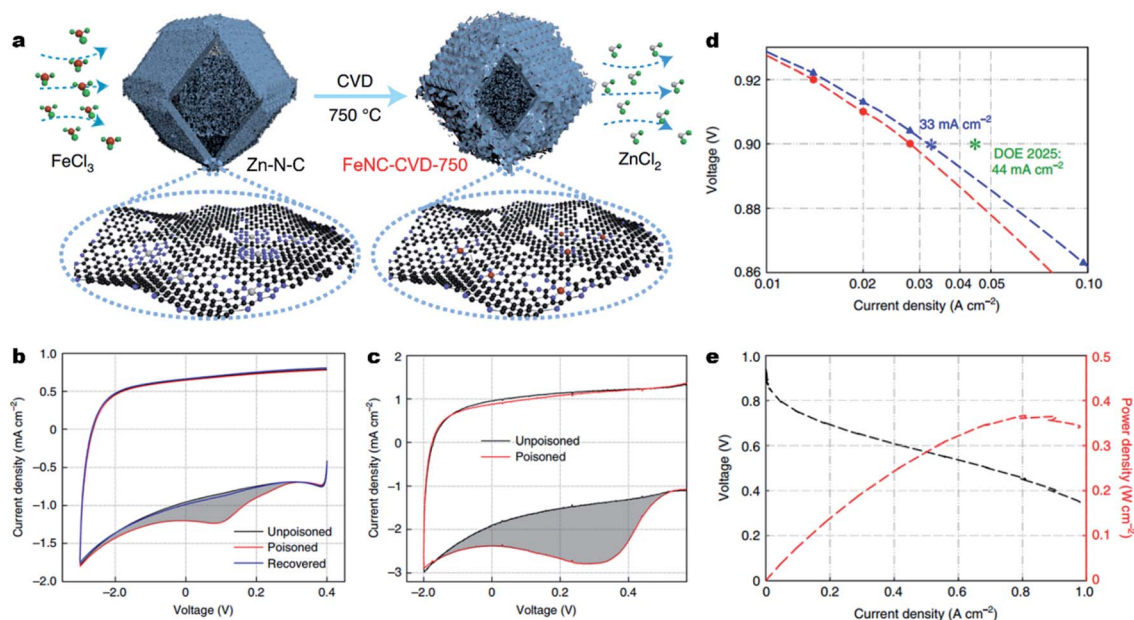


**Fig. 8** Engineering fully accessible Fe–N<sub>x</sub> sites on the surface of carbons. (a) Synthesis of FeNC-CVD-750 via an FeCl<sub>3</sub> CVD method. Red, green, grey, purple, and black balls represent Fe, Cl, Zn, N and C atoms, respectively. (b) Nitrite stripping voltammogram in N<sub>2</sub>-saturated 0.5 M acetate electrolyte buffer (pH 5.2) with a catalyst loading of 270 μg cm<sup>−2</sup> and a scan rate of 10 mV s<sup>−1</sup>. (c) NO stripping voltammogram in N<sub>2</sub>-saturated 0.5 M H<sub>2</sub>SO<sub>4</sub> with a catalyst loading of 600 μg cm<sup>−2</sup> and a scan rate of 10 mV s<sup>−1</sup>. The grey shading represents the excess current associated with the reductive stripping of nitrite. (d) Tafel plot for the determination of FeNC-CVD-750 activity at 0.9 V<sub>iR-free</sub>. (e) The H<sub>2</sub>–air PEMFC polarization curve and power density without iR-correction for the membrane electrode assembly. Conditions: 500 ml min<sup>−1</sup> H<sub>2</sub> and 2000 ml min<sup>−1</sup> air, 100% RH, 1.0 bar H<sub>2</sub> and air partial pressure, and 80 °C. Reproduced with the permission from ref. 206. Copyright (2021) Springer Nature.



**Table 1** Improve the intrinsic activity of the M–N<sub>x</sub> site for representative M–N–C electrocatalysts *via* different methods and their catalytic ORR activity

Method	M–N–C electrocatalyst	Active site	Electrolyte	$E_{\text{onset}}$ (V vs. RHE)	$E_{1/2}$ (V vs. RHE)	Ref.
Local coordination	HP-Fe–N <sub>4</sub>	Pyrrole-type Fe–N <sub>4</sub>	0.5 M H <sub>2</sub> SO <sub>4</sub>	0.95	0.80	97
	Fe–N/P–C-700	Fe–N <sub>3</sub> P <sub>1</sub>	0.1 M KOH	0.941	0.867	104
	S–Cu–ISA/SNC	Cu–N <sub>3</sub> S <sub>1</sub>	0.1 M KOH	~0.98	0.918	105
	Mn/C–NO	Mn–N <sub>3</sub> O	0.1 M KOH	~0.98	0.86	109
	Co <sub>1</sub> –SAC	Co–N <sub>3</sub> C <sub>1</sub>	0.1 M KOH	0.904	0.824	106
Heteroatom incorporation	Fe/N/C–SCN	S-modified Fe–N <sub>4</sub>	0.1 M H <sub>2</sub> SO <sub>4</sub>	—	0.836	123
	Fe–ISA/SNC	S-modified Fe–N <sub>4</sub>	0.1 M KOH	~0.98	0.896	124
	Fe–SAs/NPS–HC	S, P-co-modified Fe–N <sub>4</sub>	0.1 M KOH	~0.98	0.912	129
Axial ligand modification	Mn–N–C–S	S-modified Mn–N <sub>4</sub>	0.5 M H <sub>2</sub> SO <sub>4</sub>	~0.89	0.791	131
	FeCl <sub>1</sub> N <sub>4</sub> /CNS	Fe–Cl <sub>1</sub> N <sub>4</sub>	0.5 M H <sub>2</sub> SO <sub>4</sub>	~0.98	0.81	138
	Fe–N–C	Self-adjusted FeN <sub>4</sub> –OH	0.1 M KOH	~0.97	0.921	142
Dual metal sites	(Fe,Co)/N–C	FeN <sub>3</sub> –CoN <sub>4</sub>	0.1 M KOH	~0.97	~0.90	142
	FeCoN <sub>x</sub> /C	FeCoN <sub>5</sub> –OH	0.1 M HClO <sub>4</sub>	1.060	0.863	154
	Fe, Mn/N–C	Fe–Mn–N <sub>6</sub>	0.1 M HClO <sub>4</sub>	1.02	0.86	151
Regulation of the carbon skeleton geometry	Fe <sub>2</sub> –N–C	Fe <sub>2</sub> –N <sub>6</sub>	0.1 M HClO <sub>4</sub>	~0.92	0.804	155
	Fe–N–C (1.5Fe–ZIF)	Fe–N <sub>4</sub> –C <sub>8</sub> dominated	0.1 M KOH	~0.99	0.928	157
	FeN <sub>x</sub> /GM	Edge FeN <sub>4</sub>	0.5 M H <sub>2</sub> SO <sub>4</sub>	~0.92	0.78	161
	Fe–N <sub>4</sub> –C-60	Edge FeN <sub>4</sub>	0.5 M H <sub>2</sub> SO <sub>4</sub>	~0.98	0.88	163
	ZIF–NC–0.5Fe–700	Contracted FeN <sub>4</sub>	0.1 M HClO <sub>4</sub>	~0.90	0.80	162
			0.5 M H <sub>2</sub> SO <sub>4</sub>	~0.95	0.80	162
			0.5 M H <sub>2</sub> SO <sub>4</sub>	~0.98	0.84	112

utilization around 100%. As a result, in a 0.5 M H<sub>2</sub>SO<sub>4</sub> electrolyte, the FeNC-CVD-750 displayed excellent high ORR activity with an  $E_{1/2}$  of 0.85 V (vs. RHE). When used as a cathode catalyst in a 1.0 bar H<sub>2</sub>–O<sub>2</sub> PEMFC, FeNC-CVD-750 delivered a high current density of 33 mA cm<sup>−2</sup> at 0.90 V<sub>IR-free</sub>, which approached the DOE 2025 target of 44 mA cm<sup>−2</sup> (Fig. 8d). In 1.0 bar H<sub>2</sub>–air, the FeNC-CVD-750 delivered a  $P_{\text{max}}$  of 0.37 W cm<sup>−2</sup> (Fig. 8e), among the highest values reported for PGM-free cathodes to date. Other similar studies also reported the synthesis of Fe–N–C materials with a surface-hosted Fe–N<sub>4</sub> site, achieving high site densities, high site utilization and eventually excellent ORR performance.<sup>207,208</sup>

In short, engineering hierarchically porous carbon nanostructures and manipulating the location of M–N<sub>x</sub> sites can improve the site density, expose each active site accessible to reactants, and facilitate mass transfer, therefore promoting the ORR performance of M–N–C electrocatalysts.

## 4. Conclusions and perspectives

Single-atom carbonaceous M–N–C electrocatalysts have demonstrated promising catalytic ORR properties for applications in Zn–air batteries and PEMFCs due to their abundant resources, low cost, large surface area, structural tunability, *etc.* In this Perspective, we summarized two strategies for the preparation of high-performance M–N–C electrocatalysts toward the ORR, including increasing the intrinsic activity and promoting the accessibility of the M–N<sub>x</sub> active sites. Manipulating the coordination geometry, doping heteroatoms, constructing dual-metal sites, and regulating the geometry of the carbon skeleton can effectively engineer the electronic structure of the single metal site, thus altering the adsorption behavior of O-containing intermediates and enhancing the intrinsic

activity. Engineering carbon nanostructures can largely facilitate the exposure of the M–N<sub>x</sub> site, hence increasing the site utilization and the overall catalytic activity. In alkaline media, the as-developed M–N–C materials show superb ORR performance, outperforming that of commercial Pt/C ( $E_{1/2} \approx 0.85$  V) (Table 1). These M–N–C electrocatalysts enabled the as-assembled metal–air batteries with high energy density and efficiency. However, in acidic media, M–N–C materials are still inferior to the benchmark Pt/C ( $E_{1/2} \approx 0.85$  V) (Table 1), restricting their utilization in practical PEMFCs. Therefore, rational design of highly active M–N<sub>x</sub> sites, and fruitful identification of the active site and development of new synthetic methods for single-atom carbonaceous M–N–C electrocatalysts are still highly desirable for future practical applications. Below we provide our perspectives regarding the future directions of M–N–C electrocatalysts for the ORR.

(1) Precise active structures are the prerequisite for exploring the structure–activity relationship. However, until now, most single-atom carbonaceous M–N–C materials have been synthesized *via* high-temperature pyrolysis, which makes the synthesis process uncontrollable and thus the active structures elusive. These uncontrolled structures in M–N–C electrocatalysts further make it challenging to identify active sites and correlate the relationship between the catalyst structure and the ORR performance. Thus, the exploration of well-structure-controlled chemical methodologies and precise control of the active sites at the atomic level are essential for the development of M–N–C electrocatalysts. Furthermore, a profound understanding of the structural transformation and M–N<sub>x</sub> site formation is essential to explore more advanced catalysts. Apart from the high temperature pyrolysis process, bottom-up synthesis is a promising strategy to construct well defined active sites. Conductive MOFs, covalent organic frameworks (COFs) and other



supramolecular structures with well-defined M–N<sub>x</sub> sites might provide a promising platform for the investigation, while significant efforts are required to improve their intrinsic activity and stability.

(2) In recent years, various advanced atomic-resolution techniques including HRTEM, XAS, <sup>57</sup>Fe Mössbauer spectroscopy and DFT calculations have been used to identify the active sites of M–N–C electrocatalysts. However, they could only give the average structure information and the local structure around the single metal sites remains unclear. Thus, deeper insights into the electronic structure and geometric configuration of M–N–C electrocatalysts are still required, such as probing the local coordination environments of centrally active metal sites (*e.g.*, coordination numbers, distances, and adjacent atomic species). Further, the development of *in situ* characterization techniques, such as *in situ* electron microscopy, *in situ* XAS and *in situ* <sup>57</sup>Fe Mössbauer spectroscopy is essential for providing insight into the active site formation mechanism. In addition, detailed *in situ* or *operando* measurements are necessary to deeply reveal the real interactions between the metal centers and O-containing species (*i.e.*, O<sub>2</sub>, OOH\*, O\* and OH\*) under working potential conditions. The insightful identification of the active sites and understanding the structure–performance relationship thus can guide the further rational design of highly active M–N–C electrocatalysts.

(3) The highly active M–N<sub>x</sub> sites for the ORR are always essential. The rational design of advanced catalytically active sites and regulating their intrinsic activity are two fundamental approaches for promoting the sluggish ORR kinetics. The theoretical prediction can be used to guide the precise active site design, relying on the exploration of new synthetic approaches, such as supramolecular assembly or a new templating/confinement strategy.

(4) It has been reported that adsorption energies of OH\* and OOH\* on the active site follow the universally established scaling relationship, that is,  $\Delta G_{\text{OOH}^*} = \Delta G_{\text{OH}^*} + 3.2 \pm 0.2$ .<sup>209,210</sup> Overcoming or breaking the adsorption-energy scaling relationship is vital to enhance the ORR activity, requiring novel exemplification for catalyst design by the combination of computational screening, machine learning and experimental accumulation.

(5) To date, the developed M–N–C catalysts demonstrated excellent ORR activity in alkaline electrolytes, which enabled their superior performances in primary Zn–air batteries. However, the oxygen evolution reaction (OER) performances of such M–N–C were extremely poor, which seriously limited them as bifunctional electrocatalysts to drive the operation of a rechargeable Zn–air battery. Hence, the development of highly active and stable bifunctional electrocatalysts that alternately promote the OER and ORR kinetics is necessary. In this regard, the integration of OER-active atomic transition metals (*e.g.*, Ru, Rh or Ni) into ORR active M–N–C electrocatalysts may provide a potential approach for the exploration of bifunctional single-atom carbonaceous electrocatalysts.

(6) The reactant (*i.e.*, O<sub>2</sub>, OOH\*, O\* and OH\*) accessible number of active sites plays a key role in the ORR process. Smart design of M–N–C materials with high single metal loading is

highly necessary. Exploring new synthetic approaches *via* precursor design, supramolecular assembly and a new templating/confinement strategy is effective for achieving this target. Further, constructing porous carbon with a high specific surface area, a large porous structure and a tailored reaction interface can be flexible for facilitating the accessibility of the active site.

(7) For single-atom carbonaceous M–N–C electrocatalysts, translating their activity and stability observed in rotating disc electrode (RDE) tests into high performance devices remains a great challenge due to the lack of accurate nanoscale control of three-phase interfaces within electrodes. For the most promising PEMFC applications, developing new approaches for implementing the most promising Fe–N–C or Co–N–C electrocatalysts into membrane electrode assembly is required for achieving high PEMFC performance. Construction of hierarchically porous nanostructures with micro-porosity, meso-porosity and macro-porosity is an effective approach for achieving high MEA performance. Thereinto, micropores are capable of a high density of single metal active sites. Mesopores and macropores can promote the ionomer distribution and facilitate the mass transport.

(8) Aside from intrinsic activity, durability is another important parameter for M–N–C electrocatalysts in practical PEMFC applications. Acidic electrolytes might cause metal centers to be exchanged by protons, degrade the carbon support, and result in significant activity loss, especially for single atom Fe–N–C electrocatalysts due to the undesired Fenton reaction. Experimental and theoretical studies should focus on single metal site dissolution and carbon corrosion mechanisms. Furthermore, developing advanced supporting materials with high conductivity and corrosion resistance of M–N–C electrocatalysts are highly desirable for practical implementation.

Overall, active site engineering of single atom M–N–C electrocatalysts for the ORR is imperative to promote metal–air batteries and PEMFC technologies. It is expected that active site engineering *via* further advanced site design, modulation, and population will realize M–N–C materials for practical commercial use in the future.

## Author contributions

G. C. and X. F. formulated the project and wrote the manuscript. G. C. and H. Z. conducted a literature review and all authors contributed to revising the manuscript.

## Conflicts of interest

There are no conflicts to declare.

## Acknowledgements

This work was financially supported by the European Research Council (ERC) under the European Union's Horizon 2020 research and innovation programme (grant agreement no. 819698 and GrapheneCore3: 881603), Deutsche



Forschungsgemeinschaft (COORNETS, SPP 1928 and CRC 1415: 417590517).

## References

- 1 Y. Huang, M. Zhu, Y. Huang, Z. Pei, H. Li, Z. Wang, Q. Xue and C. Zhi, *Adv. Mater.*, 2016, **28**, 8344–8364.
- 2 Z. P. Cano, D. Banham, S. Ye, A. Hintennach, J. Lu, M. Fowler and Z. Chen, *Nat. Energy*, 2018, **3**, 279–289.
- 3 A. Kulkarni, S. Siahrostami, A. Patel and J. K. Nørskov, *Chem. Rev.*, 2018, **118**, 2302–2312.
- 4 B. Wang, *J. Power Sources*, 2005, **152**, 1–15.
- 5 X. Tian, X. F. Lu, B. Y. Xia and X. W. Lou, *Joule*, 2020, **4**, 45–68.
- 6 M. Shao, Q. Chang, J.-P. Dodelet and R. Chenitz, *Chem. Rev.*, 2016, **116**, 3594–3657.
- 7 K. Jiao, J. Xuan, Q. Du, Z. Bao, B. Xie, B. Wang, Y. Zhao, L. Fan, H. Wang, Z. Hou, S. Huo, N. P. Brandon, Y. Yin and M. D. Guiver, *Nature*, 2021, **595**, 361–369.
- 8 M. M. Tellez-Cruz, J. Escorihuela, O. Solorza-Feria and V. Compañ, *Polymers*, 2021, **13**, 3064.
- 9 G. Chen, J. Zhang, F. Wang, L. Wang, Z. Liao, E. Zschech, K. Müllen and X. Feng, *Chem.–Eur. J.*, 2018, **24**, 18413–18418.
- 10 Q. Wang, L. Shang, D. Sun-Waterhouse, T. Zhang and G. Waterhouse, *SmartMat*, 2021, **2**, 154–175.
- 11 Y.-J. Wang, N. Zhao, B. Fang, H. Li, X. T. Bi and H. Wang, *Chem. Rev.*, 2015, **115**, 3433–3467.
- 12 C. Zhu, H. Li, S. Fu, D. Du and Y. Lin, *Chem. Soc. Rev.*, 2016, **45**, 517–531.
- 13 Y. Zhou, X. Tao, G. Chen, R. Lu, D. Wang, M.-X. Chen, E. Jin, J. Yang, H.-W. Liang, Y. Zhao, X. Feng, A. Narita and K. Müllen, *Nat. Commun.*, 2020, **11**, 5892.
- 14 S. Guo, S. Zhang and S. Sun, *Angew. Chem., Int. Ed.*, 2013, **52**, 8526–8544.
- 15 L. Dai, Y. Xue, L. Qu, H.-J. Choi and J.-B. Baek, *Chem. Rev.*, 2015, **115**, 4823–4892.
- 16 Y. Nie, L. Li and Z. Wei, *Chem. Soc. Rev.*, 2015, **44**, 2168–2201.
- 17 A. A. Gewirth, J. A. Varnell and A. M. DiAscro, *Chem. Rev.*, 2018, **118**, 2313–2339.
- 18 G. Chen, T. Wang, P. Liu, Z. Liao, H. Zhong, G. Wang, P. Zhang, M. Yu, E. Zschech, M. Chen, J. Zhang and X. Feng, *Energy Environ. Sci.*, 2020, **13**, 2849–2855.
- 19 G. Chen, T. Wang, J. Zhang, P. Liu, H. Sun, X. Zhuang, M. Chen and X. Feng, *Adv. Mater.*, 2018, **30**, 1706279.
- 20 Z. Ma, Z. P. Cano, A. Yu, Z. Chen, G. Jiang, X. Fu, L. Yang, T. Wu, Z. Bai and J. Lu, *Angew. Chem., Int. Ed.*, 2020, **59**, 18334–18348.
- 21 Y. Chen, S. Ji, C. Chen, Q. Peng, D. Wang and Y. Li, *Joule*, 2018, **2**, 1242–1264.
- 22 Z. Li, S. Ji, Y. Liu, X. Cao, S. Tian, Y. Chen, Z. Niu and Y. Li, *Chem. Rev.*, 2020, **120**, 623–682.
- 23 F. Jaouen, E. Proietti, M. Lefèvre, R. Chenitz, J.-P. Dodelet, G. Wu, H. T. Chung, C. M. Johnston and P. Zelenay, *Energy Environ. Sci.*, 2011, **4**, 114–130.
- 24 F. D. Speck, J. H. Kim, G. Bae, S. H. Joo, K. J. J. Mayrhofer, C. H. Choi and S. Cherevko, *JACS Au*, 2021, **1**, 1086–1100.
- 25 Y. Han, Y.-G. Wang, W. Chen, R. Xu, L. Zheng, J. Zhang, J. Luo, R.-A. Shen, Y. Zhu, W.-C. Cheong, C. Chen, Q. Peng, D. Wang and Y. Li, *J. Am. Chem. Soc.*, 2017, **139**, 17269–17272.
- 26 T. Asset and P. Atanassov, *Joule*, 2020, **4**, 33–44.
- 27 Z. Chen, D. Higgins, A. Yu, L. Zhang and J. Zhang, *Energy Environ. Sci.*, 2011, **4**, 3167–3192.
- 28 H. Fei, J. Dong, Y. Feng, C. S. Allen, C. Wan, B. Voloskiy, M. Li, Z. Zhao, Y. Wang, H. Sun, P. An, W. Chen, Z. Guo, C. Lee, D. Chen, I. Shakir, M. Liu, T. Hu, Y. Li, A. I. Kirkland, X. Duan and Y. Huang, *Nat. Catal.*, 2018, **1**, 63–72.
- 29 B. Peng, H. Liu, Z. Liu, X. Duan and Y. Huang, *J. Phys. Chem. Lett.*, 2021, **12**, 2837–2847.
- 30 B. Bayatsarmadi, Y. Zheng, A. Vasileff and S.-Z. Qiao, *Small*, 2017, **13**, 1700191.
- 31 U. Martinez, S. Komini Babu, E. F. Holby, H. T. Chung, X. Yin and P. Zelenay, *Adv. Mater.*, 2019, **31**, 1806545.
- 32 R. Jasinski, *Nature*, 1964, **201**, 1212–1213.
- 33 V. S. Bagotzky, M. R. Tarasevich, K. A. Radyushkina, O. A. Levina and S. I. Andrusyova, *J. Power Sources*, 1978, **2**, 233–240.
- 34 J. A. R. van Veen, J. F. van Baar and K. J. Kroese, *J. Chem. Soc., Faraday Trans.*, 1981, **77**, 2827–2843.
- 35 T. Sun, B. Tian, J. Lu and C. Su, *J. Mater. Chem. A*, 2017, **5**, 18933–18950.
- 36 G. Wu and P. Zelenay, *Acc. Chem. Res.*, 2013, **46**, 1878–1889.
- 37 Y. He, Q. Tan, L. Lu, J. Sokolowski and G. Wu, *Electrochem. Energy Rev.*, 2019, **2**, 231–251.
- 38 D. Zhao, Z. Zhuang, X. Cao, C. Zhang, Q. Peng, C. Chen and Y. Li, *Chem. Soc. Rev.*, 2020, **49**, 2215–2264.
- 39 H. Zhang, H. Osgood, X. Xie, Y. Shao and G. Wu, *Nano Energy*, 2017, **31**, 331–350.
- 40 M. Lefèvre, J. P. Dodelet and P. Bertrand, *J. Phys. Chem. B*, 2000, **104**, 11238–11247.
- 41 M. Lefèvre, J. P. Dodelet and P. Bertrand, *J. Phys. Chem. B*, 2002, **106**, 8705–8713.
- 42 X. Wan, W. Chen, J. Yang, M. Liu, X. Liu and J. Shui, *ChemElectroChem*, 2019, **6**, 304–315.
- 43 V. A. Saveleva, K. Ebner, L. Ni, G. Smolentsev, D. Klose, A. Zitolo, E. Marelli, J. Li, M. Medarde, O. V. Safonova, M. Nachttegaal, F. Jaouen, U. I. Kramm, T. J. Schmidt and J. Herranz, *Angew. Chem., Int. Ed.*, 2021, **60**, 11707–11712.
- 44 U. I. Kramm, L. Ni and S. Wagner, *Adv. Mater.*, 2019, **31**, 1805623.
- 45 J. M. Thomas, *Proc.: Math., Phys. Eng. Sci.*, 2017, **473**, 20160714.
- 46 H. T. Chung, D. A. Cullen, D. Higgins, B. T. Sneed, E. F. Holby, K. L. More and P. Zelenay, *Science*, 2017, **357**, 479–484.
- 47 Y. Zhao, G. I. N. Waterhouse, G. Chen, X. Xiong, L. Z. Wu, C. H. Tung and T. Zhang, *Chem. Soc. Rev.*, 2019, **48**, 1972–2010.
- 48 S. Zhao, C. Tan, C.-T. He, P. An, F. Xie, S. Jiang, Y. Zhu, K.-H. Wu, B. Zhang, H. Li, J. Zhang, Y. Chen, S. Liu, J. Dong and Z. Tang, *Nat. Energy*, 2020, **5**, 881–890.



- 49 Q. Jia, E. Liu, L. Jiao, S. Pann and S. Mukerjee, *Adv. Mater.*, 2019, **31**, 1805157.
- 50 A. Zitolo, V. Goellner, V. Armel, M.-T. Sougrati, T. Mineva, L. Stievano, E. Fonda and F. Jaouen, *Nat. Mater.*, 2015, **14**, 937.
- 51 P. Yin, T. Yao, Y. Wu, L. Zheng, Y. Lin, W. Liu, H. Ju, J. Zhu, X. Hong, Z. Deng, G. Zhou, S. Wei and Y. Li, *Angew. Chem., Int. Ed.*, 2016, **55**, 10800–10805.
- 52 A. Zitolo, N. Ranjbar-Sahraie, T. Mineva, J. Li, Q. Jia, S. Stamatina, G. F. Harrington, S. M. Lyth, P. Krttil, S. Mukerjee, E. Fonda and F. Jaouen, *Nat. Commun.*, 2017, **8**, 957.
- 53 Z. Miao, Y. Xia, J. Liang, L. Xie, S. Chen, S. Li, H.-L. Wang, S. Hu, J. Han and Q. Li, *Small*, 2021, **17**, 2100735.
- 54 H. Zhang, W. Zhou, T. Chen, B. Y. Guan, Z. Li and X. W. Lou, *Energy Environ. Sci.*, 2018, **11**, 1980–1984.
- 55 J. Li, M. Chen, D. A. Cullen, S. Hwang, M. Wang, B. Li, K. Liu, S. Karakalos, M. Lucero, H. Zhang, C. Lei, H. Xu, G. E. Sterbinsky, Z. Feng, D. Su, K. L. More, G. Wang, Z. Wang and G. Wu, *Nat. Catal.*, 2018, **1**, 935–945.
- 56 X. Xiong, Y. Li, Y. Jia, Y. Meng, K. Sun, L. Zheng, G. Zhang, Y. Li and X. Sun, *Nanoscale*, 2019, **11**, 15900–15906.
- 57 Q. Zhou, J. Cai, Z. Zhang, R. Gao, B. Chen, G. Wen, L. Zhao, Y. Deng, H. Dou, X. Gong, Y. Zhang, Y. Hu, A. Yu, X. Sui, Z. Wang and Z. Chen, *Small Methods*, 2021, **5**, 2100024.
- 58 J. Wang, H. Li, S. Liu, Y. Hu, J. Zhang, M. Xia, Y. Hou, J. Tse, J. Zhang and Y. Zhao, *Angew. Chem., Int. Ed.*, 2021, **60**, 181–185.
- 59 Z. Jiang, W. Sun, H. Shang, W. Chen, T. Sun, H. Li, J. Dong, J. Zhou, Z. Li, Y. Wang, R. Cao, R. Sarangi, Z. Yang, D. Wang, J. Zhang and Y. Li, *Energy Environ. Sci.*, 2019, **12**, 3508–3514.
- 60 F. Li, G.-F. Han, H.-J. Noh, S.-J. Kim, Y. Lu, H. Y. Jeong, Z. Fu and J.-B. Baek, *Energy Environ. Sci.*, 2018, **11**, 2263–2269.
- 61 S. Ji, Y. Chen, X. Wang, Z. Zhang, D. Wang and Y. Li, *Chem. Rev.*, 2020, **120**, 11900–11955.
- 62 M.-X. Chen, M. Zhu, M. Zuo, S.-Q. Chu, J. Zhang, Y. Wu, H.-W. Liang and X. Feng, *Angew. Chem., Int. Ed.*, 2020, **59**, 1627–1633.
- 63 G. Wu, K. L. More, C. M. Johnston and P. Zelenay, *Science*, 2011, **332**, 443–447.
- 64 J. Guo, J. Huo, Y. Liu, W. Wu, Y. Wang, M. Wu, H. Liu and G. Wang, *Small Methods*, 2019, **3**, 1900159.
- 65 L. Zhao, Y. Zhang, L.-B. Huang, X.-Z. Liu, Q.-H. Zhang, C. He, Z.-Y. Wu, L.-J. Zhang, J. Wu, W. Yang, L. Gu, J.-S. Hu and L.-J. Wan, *Nat. Commun.*, 2019, **10**, 1278.
- 66 G. Zhang, Y. Jia, C. Zhang, X. Xiong, K. Sun, R. Chen, W. Chen, Y. Kuang, L. Zheng, H. Tang, W. Liu, J. Liu, X. Sun, W.-F. Lin and H. Dai, *Energy Environ. Sci.*, 2019, **12**, 1317–1325.
- 67 Z. Song, L. Zhang, K. Doyle-Davis, X. Fu, J.-L. Luo and X. Sun, *Adv. Energy Mater.*, 2020, **10**, 2001561.
- 68 A. Han, B. Wang, A. Kumar, Y. Qin, J. Jin, X. Wang, C. Yang, B. Dong, Y. Jia, J. Liu and X. Sun, *Small Methods*, 2019, **3**, 1800471.
- 69 L. Li, J. He, Y. Wang, X. Lv, X. Gu, P. Dai, D. Liu and X. Zhao, *J. Mater. Chem. A*, 2019, **7**, 1964–1988.
- 70 L. Jiao, G. Wan, R. Zhang, H. Zhou, S.-H. Yu and H.-L. Jiang, *Angew. Chem., Int. Ed.*, 2018, **57**, 8525–8529.
- 71 H.-F. Wang, L. Chen, H. Pang, S. Kaskel and Q. Xu, *Chem. Soc. Rev.*, 2020, **49**, 1414–1448.
- 72 Y.-S. Wei, M. Zhang, R. Zou and Q. Xu, *Chem. Rev.*, 2020, **120**, 12089–12174.
- 73 C. Zhu, Q. Shi, B. Z. Xu, S. Fu, G. Wan, C. Yang, S. Yao, J. Song, H. Zhou, D. Du, S. P. Beckman, D. Su and Y. Lin, *Adv. Energy Mater.*, 2018, **8**, 1801956.
- 74 Y. Chen, Z. Li, Y. Zhu, D. Sun, X. Liu, L. Xu and Y. Tang, *Adv. Mater.*, 2019, **31**, 1806312.
- 75 M. Chen, Y. He, J. S. Spendelow and G. Wu, *ACS Energy Lett.*, 2019, **4**, 1619–1633.
- 76 M. Liu, L. Wang, K. Zhao, S. Shi, Q. Shao, L. Zhang, X. Sun, Y. Zhao and J. Zhang, *Energy Environ. Sci.*, 2019, **12**, 2890–2923.
- 77 Y. Wang, H. Su, Y. He, L. Li, S. Zhu, H. Shen, P. Xie, X. Fu, G. Zhou, C. Feng, D. Zhao, F. Xiao, X. Zhu, Y. Zeng, M. Shao, S. Chen, G. Wu, J. Zeng and C. Wang, *Chem. Rev.*, 2020, **120**, 12217–12314.
- 78 E. Luo, Y. Chu, J. Liu, Z. Shi, S. Zhu, L. Gong, J. Ge, C. H. Choi, C. Liu and W. Xing, *Energy Environ. Sci.*, 2021, **14**, 2158–2185.
- 79 M.-X. Chen, L. Tong and H.-W. Liang, *Chem.–Eur. J.*, 2021, **27**, 145–157.
- 80 J. Zhang, G. Chen, K. Müllen and X. Feng, *Adv. Mater.*, 2018, **30**, 1800528.
- 81 Y. Wang, F. Chu, J. Zeng, Q. Wang, T. Naren, Y. Li, Y. Cheng, Y. Lei and F. Wu, *ACS Nano*, 2021, **15**, 210–239.
- 82 X. X. Wang, M. T. Swihart and G. Wu, *Nat. Catal.*, 2019, **2**, 578–589.
- 83 C.-X. Zhao, B.-Q. Li, J.-N. Liu and Q. Zhang, *Angew. Chem., Int. Ed.*, 2021, **60**, 4448–4463.
- 84 W.-H. Lai, Z. Miao, Y.-X. Wang, J.-Z. Wang and S.-L. Chou, *Adv. Energy Mater.*, 2019, **9**, 1900722.
- 85 T. Sun, S. Mitchell, J. Li, P. Lyu, X. Wu, J. Pérez-Ramírez and J. Lu, *Adv. Mater.*, 2021, **33**, 2003075.
- 86 H. Peng, F. Liu, X. Liu, S. Liao, C. You, X. Tian, H. Nan, F. Luo, H. Song, Z. Fu and P. Huang, *ACS Catal.*, 2014, **4**, 3797–3805.
- 87 Y. Zheng, D.-S. Yang, J. M. Kweun, C. Li, K. Tan, F. Kong, C. Liang, Y. J. Chabal, Y. Y. Kim, M. Cho, J.-S. Yu and K. Cho, *Nano Energy*, 2016, **30**, 443–449.
- 88 F. Calle-Vallejo, J. I. Martínez and J. Rossmeisl, *Phys. Chem. Chem. Phys.*, 2011, **13**, 15639–15643.
- 89 J. Masa, A. Zhao, W. Xia, M. Muhler and W. Schuhmann, *Electrochim. Acta*, 2014, **128**, 271–278.
- 90 L. Osmieri, A. H. A. Monteverde Videla, P. Ocón and S. Specchia, *J. Phys. Chem. C*, 2017, **121**, 17796–17817.
- 91 J. Kim, J. M. Yoo, H. S. Lee, Y.-E. Sung and T. Hyeon, *Trends Chem.*, 2021, **3**, 779–794.
- 92 Z. W. Seh, J. Kibsgaard, C. F. Dickens, I. Chorkendorff, J. K. Nørskov and T. F. Jaramillo, *Science*, 2017, **355**, eaad4998.
- 93 Y. He, S. Liu, C. Priest, Q. Shi and G. Wu, *Chem. Soc. Rev.*, 2020, **49**, 3484–3524.





- 94 J. Qin, Z. Liu, D. Wu and J. Yang, *Appl. Catal., B*, 2020, **278**, 119300.
- 95 U. I. Kramm, J. Herranz, N. Larouche, T. M. Arruda, M. Lefèvre, F. Jaouen, P. Bogdanoff, S. Fiechter, I. Abs-Wurmbach, S. Mukerjee and J.-P. Dodelet, *Phys. Chem. Chem. Phys.*, 2012, **14**, 11673–11688.
- 96 L. Yang, D. Cheng, H. Xu, X. Zeng, X. Wan, J. Shui, Z. Xiang and D. Cao, *Proc. Natl. Acad. Sci. U. S. A.*, 2018, **115**, 6626–6631.
- 97 N. Zhang, T. Zhou, M. Chen, H. Feng, R. Yuan, C. a. Zhong, W. Yan, Y. Tian, X. Wu, W. Chu, C. Wu and Y. Xie, *Energy Environ. Sci.*, 2020, **13**, 111–118.
- 98 J. Li, M. T. Sougrati, A. Zitolo, J. M. Ablett, I. C. Oğuz, T. Mineva, I. Matanovic, P. Atanassov, Y. Huang, I. Zenyuk, A. Di Cicco, K. Kumar, L. Dubau, F. Maillard, G. Dražić and F. Jaouen, *Nat. Catal.*, 2021, **4**, 10–19.
- 99 J. Zhang, H. Yang and B. Liu, *Adv. Energy Mater.*, 2021, **11**, 2002473.
- 100 M. Wang, W. Yang, X. Li, Y. Xu, L. Zheng, C. Su and B. Liu, *ACS Energy Lett.*, 2021, **6**, 379–386.
- 101 X. Zhu, X. Tan, K.-H. Wu, C.-L. Chiang, Y.-C. Lin, Y.-G. Lin, D.-W. Wang, S. Smith, X. Lu and R. Amal, *J. Mater. Chem. A*, 2019, **7**, 14732–14742.
- 102 X. Li, L. Liu, X. Ren, J. Gao, Y. Huang and B. Liu, *Sci. Adv.*, 2020, **6**, eabb6833.
- 103 X. Li, H. Rong, J. Zhang, D. Wang and Y. Li, *Nano Res.*, 2020, **13**, 1842–1855.
- 104 K. Yuan, D. Lützenkirchen-Hecht, L. Li, L. Shuai, Y. Li, R. Cao, M. Qiu, X. Zhuang, M. K. H. Leung, Y. Chen and U. Scherf, *J. Am. Chem. Soc.*, 2020, **142**, 2404–2412.
- 105 H. Shang, X. Zhou, J. Dong, A. Li, X. Zhao, Q. Liu, Y. Lin, J. Pei, Z. Li, Z. Jiang, D. Zhou, L. Zheng, Y. Wang, J. Zhou, Z. Yang, R. Cao, R. Sarangi, T. Sun, X. Yang, X. Zheng, W. Yan, Z. Zhuang, J. Li, W. Chen, D. Wang, J. Zhang and Y. Li, *Nat. Commun.*, 2020, **11**, 3049.
- 106 X. Hai, X. Zhao, N. Guo, C. Yao, C. Chen, W. Liu, Y. Du, H. Yan, J. Li, Z. Chen, X. Li, Z. Li, H. Xu, P. Lyu, J. Zhang, M. Lin, C. Su, S. J. Pennycook, C. Zhang, S. Xi and J. Lu, *ACS Catal.*, 2020, **10**, 5862–5870.
- 107 Y. Ha, B. Fei, X. Yan, H. Xu, Z. Chen, L. Shi, M. Fu, W. Xu and R. Wu, *Adv. Energy Mater.*, 2020, **10**, 2002592.
- 108 F. Li, G.-F. Han, Y. Bu, H.-J. Noh, J.-P. Jeon, T. J. Shin, S.-J. Kim, Y. Wu, H. Y. Jeong, Z. Fu, Y. Lu and J.-B. Baek, *Angew. Chem., Int. Ed.*, 2020, **59**, 23678–23683.
- 109 Y. Yang, K. Mao, S. Gao, H. Huang, G. Xia, Z. Lin, P. Jiang, C. Wang, H. Wang and Q. Chen, *Adv. Mater.*, 2018, **30**, 1801732.
- 110 S. Liu, Z. Li, C. Wang, W. Tao, M. Huang, M. Zuo, Y. Yang, K. Yang, L. Zhang, S. Chen, P. Xu and Q. Chen, *Nat. Commun.*, 2020, **11**, 938.
- 111 J. Zhang, Y. Zhao, C. Chen, Y.-C. Huang, C.-L. Dong, C.-J. Chen, R.-S. Liu, C. Wang, K. Yan, Y. Li and G. Wang, *J. Am. Chem. Soc.*, 2019, **141**, 20118–20126.
- 112 J. Li, H. Zhang, W. Samarakoon, W. Shan, D. A. Cullen, S. Karakalos, M. Chen, D. Gu, K. L. More, G. Wang, Z. Feng, Z. Wang and G. Wu, *Angew. Chem., Int. Ed.*, 2019, **58**, 18971–18980.
- 113 Y. He, Q. Shi, W. Shan, X. Li, A. J. Kropf, E. C. Wegener, J. Wright, S. Karakalos, D. Su, D. A. Cullen, G. Wang, D. J. Myers and G. Wu, *Angew. Chem., Int. Ed.*, 2021, **60**, 9516–9526.
- 114 Y. Wang, K. Liu, J. Li, X. Yang, J. Hu, T.-S. Chan, X. Qiu, W. Li and M. Liu, *Chem. Eng. J.*, 2022, **429**, 132119.
- 115 Z. Li, Z. Zhuang, F. Lv, H. Zhu, L. Zhou, M. Luo, J. Zhu, Z. Lang, S. Feng, W. Chen, L. Mai and S. Guo, *Adv. Mater.*, 2018, **30**, 1803220.
- 116 C. Tang, Y. Jiao, B. Shi, J.-N. Liu, Z. Xie, X. Chen, Q. Zhang and S.-Z. Qiao, *Angew. Chem., Int. Ed.*, 2020, **59**, 9171–9176.
- 117 C. Tang, L. Chen, H. Li, L. Li, Y. Jiao, Y. Zheng, H. Xu, K. Davey and S.-Z. Qiao, *J. Am. Chem. Soc.*, 2021, **143**, 7819–7827.
- 118 G. Daniel, M. Mazzucato, R. Brandiele, L. De Lazzari, D. Badocco, P. Pastore, T. Kosmala, G. Granozzi and C. Durante, *ACS Appl. Mater. Interfaces*, 2021, **13**, 42693–42705.
- 119 X. Wei, X. Luo, N. Wu, W. Gu, Y. Lin and C. Zhu, *Nano Energy*, 2021, **84**, 105817.
- 120 J. Zhang, M. Zhang, Y. Zeng, J. Chen, L. Qiu, H. Zhou, C. Sun, Y. Yu, C. Zhu and Z. Zhu, *Small*, 2019, **15**, 1900307.
- 121 C. Shao, L. Wu, H. Zhang, Q. Jiang, X. Xu, Y. Wang, S. Zhuang, H. Chu, L. Sun, J. Ye, B. Li and X. Wang, *Adv. Funct. Mater.*, 2021, **31**, 2100833.
- 122 J.-C. Li, H. Zhong, M. Xu, T. Li, L. Wang, Q. Shi, S. Feng, Z. Lyu, D. Liu, D. Du, S. P. Beckman, X. Pan, Y. Lin and M. Shao, *Sci. China Mater.*, 2020, **63**, 965–971.
- 123 Y.-C. Wang, Y.-J. Lai, L. Song, Z.-Y. Zhou, J.-G. Liu, Q. Wang, X.-D. Yang, C. Chen, W. Shi, Y.-P. Zheng, M. Rauf and S.-G. Sun, *Angew. Chem., Int. Ed.*, 2015, **54**, 9907–9910.
- 124 Q. Li, W. Chen, H. Xiao, Y. Gong, Z. Li, L. Zheng, X. Zheng, W. Yan, W.-C. Cheong, R. Shen, N. Fu, L. Gu, Z. Zhuang, C. Chen, D. Wang, Q. Peng, J. Li and Y. Li, *Adv. Mater.*, 2018, **30**, 1800588.
- 125 Y. Mun, S. Lee, K. Kim, S. Kim, S. Lee, J. W. Han and J. Lee, *J. Am. Chem. Soc.*, 2019, **141**, 6254–6262.
- 126 H. Sun, S. Liu, M. Wang, T. Qian, J. Xiong and C. Yan, *ACS Appl. Mater. Interfaces*, 2019, **11**, 33054–33061.
- 127 H. Sun, M. Wang, X. Du, Y. Jiao, S. Liu, T. Qian, Y. Yan, C. Liu, M. Liao, Q. Zhang, L. Meng, L. Gu, J. Xiong and C. Yan, *J. Mater. Chem. A*, 2019, **7**, 20952–20957.
- 128 K. Yuan, S. Sfaelou, M. Qiu, D. Lützenkirchen-Hecht, X. Zhuang, Y. Chen, C. Yuan, X. Feng and U. Scherf, *ACS Energy Lett.*, 2018, **3**, 252–260.
- 129 Y. Chen, S. Ji, S. Zhao, W. Chen, J. Dong, W.-C. Cheong, R. Shen, X. Wen, L. Zheng, A. I. Rykov, S. Cai, H. Tang, Z. Zhuang, C. Chen, Q. Peng, D. Wang and Y. Li, *Nat. Commun.*, 2018, **9**, 5422.
- 130 S. Guo, P. Yuan, J. Zhang, P. Jin, H. Sun, K. Lei, X. Pang, Q. Xu and F. Cheng, *Chem. Commun.*, 2017, **53**, 9862–9865.
- 131 L. Guo, S. Hwang, B. Li, F. Yang, M. Wang, M. Chen, X. Yang, S. G. Karakalos, D. A. Cullen, Z. Feng, G. Wang, G. Wu and H. Xu, *ACS Nano*, 2021, **15**, 6886–6899.
- 132 H. Shang, Z. Jiang, D. Zhou, J. Pei, Y. Wang, J. Dong, X. Zheng, J. Zhang and W. Chen, *Chem. Sci.*, 2020, **11**, 5994–5999.



- 133 P.-J. Wei, G.-Q. Yu, Y. Naruta and J.-G. Liu, *Angew. Chem., Int. Ed.*, 2014, **53**, 6659–6663.
- 134 L. Xie, X.-P. Zhang, B. Zhao, P. Li, J. Qi, X. Guo, B. Wang, H. Lei, W. Zhang, U.-P. Apfel and R. Cao, *Angew. Chem., Int. Ed.*, 2021, **60**, 7576–7581.
- 135 A. Friedman, L. Landau, S. Gonen, Z. Gross and L. Elbaz, *ACS Catal.*, 2018, **8**, 5024–5031.
- 136 L. Gong, H. Zhang, Y. Wang, E. Luo, K. Li, L. Gao, Y. Wang, Z. Wu, Z. Jin, J. Ge, Z. Jiang, C. Liu and W. Xing, *Angew. Chem., Int. Ed.*, 2020, **59**, 13923–13928.
- 137 R. Cao, R. Thapa, H. Kim, X. Xu, M. Gyu Kim, Q. Li, N. Park, M. Liu and J. Cho, *Nat. Commun.*, 2013, **4**, 2076.
- 138 Y. Han, Y. Wang, R. Xu, W. Chen, L. Zheng, A. Han, Y. Zhu, J. Zhang, H. Zhang, J. Luo, C. Chen, Q. Peng, D. Wang and Y. Li, *Energy Environ. Sci.*, 2018, **11**, 2348–2352.
- 139 F. Wang, Y. Zhou, S. Lin, L. Yang, Z. Hu and D. Xie, *Nano Energy*, 2020, **78**, 105128.
- 140 X. Li, C.-S. Cao, S.-F. Hung, Y.-R. Lu, W. Cai, A. I. Rykov, S. Miao, S. Xi, H. Yang, Z. Hu, J. Wang, J. Zhao, E. E. Alp, W. Xu, T.-S. Chan, H. Chen, Q. Xiong, H. Xiao, Y. Huang, J. Li, T. Zhang and B. Liu, *Chem*, 2020, **6**, 3440–3454.
- 141 Y. Wang, Y.-J. Tang and K. Zhou, *J. Am. Chem. Soc.*, 2019, **141**, 14115–14119.
- 142 X. Yang, D. Xia, Y. Kang, H. Du, F. Kang, L. Gan and J. Li, *Adv. Sci.*, 2020, **7**, 2000176.
- 143 K. Chen, K. Liu, P. An, H. Li, Y. Lin, J. Hu, C. Jia, J. Fu, H. Li, H. Liu, Z. Lin, W. Li, J. Li, Y.-R. Lu, T.-S. Chan, N. Zhang and M. Liu, *Nat. Commun.*, 2020, **11**, 4173.
- 144 J. Zhu and S. Mu, *Chem. Commun.*, 2021, **57**, 7869–7881.
- 145 Z. Zhu, H. Yin, Y. Wang, C.-H. Chuang, L. Xing, M. Dong, Y.-R. Lu, G. Casillas-Garcia, Y. Zheng, S. Chen, Y. Dou, P. Liu, Q. Cheng and H. Zhao, *Adv. Mater.*, 2020, **32**, 2004670.
- 146 X. Han, X. Ling, D. Yu, D. Xie, L. Li, S. Peng, C. Zhong, N. Zhao, Y. Deng and W. Hu, *Adv. Mater.*, 2019, **31**, 1905622.
- 147 Z. Jin, P. Li, Y. Meng, Z. Fang, D. Xiao and G. Yu, *Nat. Catal.*, 2021, **4**, 615–622.
- 148 M. Tong, F. Sun, Y. Xie, Y. Wang, Y. Yang, C. Tian, L. Wang and H. Fu, *Angew. Chem., Int. Ed.*, 2021, **60**, 14005–14012.
- 149 V. Jose, H. Hu, E. Edison, W. Manalastas Jr, H. Ren, P. Kidkhunthod, S. Sreejith, A. Jayakumar, J. M. V. Nsanizimana, M. Srinivasan, J. Choi and J.-M. Lee, *Small Methods*, 2021, **5**, 2000751.
- 150 J. Wang, W. Liu, G. Luo, Z. Li, C. Zhao, H. Zhang, M. Zhu, Q. Xu, X. Wang, C. Zhao, Y. Qu, Z. Yang, T. Yao, Y. Li, Y. Lin, Y. Wu and Y. Li, *Energy Environ. Sci.*, 2018, **11**, 3375–3379.
- 151 M. Xiao, Y. Chen, J. Zhu, H. Zhang, X. Zhao, L. Gao, X. Wang, J. Zhao, J. Ge, Z. Jiang, S. Chen, C. Liu and W. Xing, *J. Am. Chem. Soc.*, 2019, **141**, 17763–17770.
- 152 D. Liu, B. Wang, H. Li, S. Huang, M. Liu, J. Wang, Q. Wang, J. Zhang and Y. Zhao, *Nano Energy*, 2019, **58**, 277–283.
- 153 H. Li, J. Wang, R. Qi, Y. Hu, J. Zhang, H. Zhao, J. Zhang and Y. Zhao, *Appl. Catal., B*, 2021, **285**, 119778.
- 154 J. Wang, Z. Huang, W. Liu, C. Chang, H. Tang, Z. Li, W. Chen, C. Jia, T. Yao, S. Wei, Y. Wu and Y. Li, *J. Am. Chem. Soc.*, 2017, **139**, 17281–17284.
- 155 G. Yang, J. Zhu, P. Yuan, Y. Hu, G. Qu, B.-A. Lu, X. Xue, H. Yin, W. Cheng, J. Cheng, W. Xu, J. Li, J. Hu, S. Mu and J.-N. Zhang, *Nat. Commun.*, 2021, **12**, 1734.
- 156 M. Xiao, H. Zhang, Y. Chen, J. Zhu, L. Gao, Z. Jin, J. Ge, Z. Jiang, S. Chen, C. Liu and W. Xing, *Nano Energy*, 2018, **46**, 396–403.
- 157 W. Ye, S. Chen, Y. Lin, L. Yang, S. Chen, X. Zheng, Z. Qi, C. Wang, R. Long, M. Chen, J. Zhu, P. Gao, L. Song, J. Jiang and Y. Xiong, *Chem*, 2019, **5**, 2865–2878.
- 158 N. Zhang, T. Zhou, J. Ge, Y. Lin, Z. Du, C. a. Zhong, W. Wang, Q. Jiao, R. Yuan, Y. Tian, W. Chu, C. Wu and Y. Xie, *Matter*, 2020, **3**, 509–521.
- 159 C. E. Szakaacs, M. Lefèvre, U. I. Kramm, J.-P. Dodelet and F. Vidal, *Phys. Chem. Chem. Phys.*, 2014, **16**, 13654–13661.
- 160 K. Liu, G. Wu and G. Wang, *J. Phys. Chem. C*, 2017, **121**, 11319–11324.
- 161 H. Zhang, H. T. Chung, D. A. Cullen, S. Wagner, U. I. Kramm, K. L. More, P. Zelenay and G. Wu, *Energy Environ. Sci.*, 2019, **12**, 2548–2558.
- 162 X. Wang, Y. Jia, X. Mao, D. Liu, W. He, J. Li, J. Liu, X. Yan, J. Chen, L. Song, A. Du and X. Yao, *Adv. Mater.*, 2020, **32**, 2000966.
- 163 X. Fu, N. Li, B. Ren, G. Jiang, Y. Liu, F. M. Hassan, D. Su, J. Zhu, L. Yang, Z. Bai, Z. P. Cano, A. Yu and Z. Chen, *Adv. Energy Mater.*, 2019, **9**, 1803737.
- 164 X. Yu, S. Lai, S. Xin, S. Chen, X. Zhang, X. She, T. Zhan, X. Zhao and D. Yang, *Appl. Catal., B*, 2021, **280**, 119437.
- 165 T. He, B. Lu, Y. Chen, Y. Wang, Y. Zhang, J. L. Davenport, A. P. Chen, C.-W. Pao, M. Liu and Z. Sun, *Research*, 2019, **2019**, 6813585.
- 166 K. Khan, X. Yan, Q. Yu, S.-H. Bae, J. J. White, J. Liu, T. Liu, C. Sun, J. Kim, H.-M. Cheng, Y. Wang, B. Liu, K. Amine, X. Pan and Z. Luo, *Nano Energy*, 2021, **90**, 106488.
- 167 Y. He, S. Hwang, D. A. Cullen, M. A. Uddin, L. Langhorst, B. Li, S. Karakalos, A. J. Kropf, E. C. Wegener, J. Sokolowski, M. Chen, D. Myers, D. Su, K. L. More, G. Wang, S. Litster and G. Wu, *Energy Environ. Sci.*, 2019, **12**, 250–260.
- 168 S. Yuan, J. Zhang, L. Hu, J. Li, S. Li, Y. Gao, Q. Zhang, L. Gu, W. Yang, X. Feng and B. Wang, *Angew. Chem., Int. Ed.*, 2021, **60**, 21685–21690.
- 169 J. Wu, H. Zhou, Q. Li, M. Chen, J. Wan, N. Zhang, L. Xiong, S. Li, B. Y. Xia, G. Feng, M. Liu and L. Huang, *Adv. Energy Mater.*, 2019, **9**, 1900149.
- 170 C. Xia, Y. Qiu, Y. Xia, P. Zhu, G. King, X. Zhang, Z. Wu, J. Y. Kim, D. A. Cullen, D. Zheng, P. Li, M. Shakouri, E. Heredia, P. Cui, H. N. Alshareef, Y. Hu and H. Wang, *Nat. Chem.*, 2021, **13**, 887–894.
- 171 H. Yin, H. Xia, S. Zhao, K. Li, J. Zhang and S. Mu, *Energy Environ. Mater.*, 2021, **4**, 5–18.
- 172 X. Wang, H. Zhang, H. Lin, S. Gupta, C. Wang, Z. Tao, H. Fu, T. Wang, J. Zheng, G. Wu and X. Li, *Nano Energy*, 2016, **25**, 110–119.
- 173 X. Xu, Z. Xia, X. Zhang, R. Sun, X. Sun, H. Li, C. Wu, J. Wang, S. Wang and G. Sun, *Appl. Catal., B*, 2019, **259**, 118042.



- 174 F. Xiao, G.-L. Xu, C.-J. Sun, M. Xu, W. Wen, Q. Wang, M. Gu, S. Zhu, Y. Li, Z. Wei, X. Pan, J. Wang, K. Amine and M. Shao, *Nano Energy*, 2019, **61**, 60–68.
- 175 X. Han, X. Ling, Y. Wang, T. Ma, C. Zhong, W. Hu and Y. Deng, *Angew. Chem., Int. Ed.*, 2019, **58**, 5359–5364.
- 176 Y. Zheng and S.-Z. Qiao, *Natl. Sci. Rev.*, 2018, **5**, 626–627.
- 177 V. Armel, S. Hindocha, F. Salles, S. Bennett, D. Jones and F. Jaouen, *J. Am. Chem. Soc.*, 2017, **139**, 453–464.
- 178 T. Al-Zoubi, Y. Zhou, X. Yin, B. Janicek, C. Sun, C. E. Schulz, X. Zhang, A. A. Gewirth, P. Huang, P. Zelenay and H. Yang, *J. Am. Chem. Soc.*, 2020, **142**, 5477–5481.
- 179 Y. Zhou, G. Chen, Q. Wang, D. Wang, X. Tao, T. Zhang, X. Feng and K. Müllen, *Adv. Funct. Mater.*, 2021, **31**, 2102420.
- 180 Q. Liu, X. Liu, L. Zheng and J. Shui, *Angew. Chem., Int. Ed.*, 2018, **57**, 1204–1208.
- 181 C.-C. Hou, H.-F. Wang, C. Li and Q. Xu, *Energy Environ. Sci.*, 2020, **13**, 1658–1693.
- 182 H. Zhang, S. Hwang, M. Wang, Z. Feng, S. Karakalos, L. Luo, Z. Qiao, X. Xie, C. Wang, D. Su, Y. Shao and G. Wu, *J. Am. Chem. Soc.*, 2017, **139**, 14143–14149.
- 183 Y. Chen, S. Ji, Y. Wang, J. Dong, W. Chen, Z. Li, R. Shen, L. Zheng, Z. Zhuang, D. Wang and Y. Li, *Angew. Chem., Int. Ed.*, 2017, **56**, 6937–6941.
- 184 J. Wang, G. Han, L. Wang, L. Du, G. Chen, Y. Gao, Y. Ma, C. Du, X. Cheng, P. Zuo and G. Yin, *Small*, 2018, **14**, 1704282.
- 185 R. Jiang, L. Li, T. Sheng, G. Hu, Y. Chen and L. Wang, *J. Am. Chem. Soc.*, 2018, **140**, 11594–11598.
- 186 J. Shan, C. Ye, S. Chen, T. Sun, Y. Jiao, L. Liu, C. Zhu, L. Song, Y. Han, M. Jaroniec, Y. Zhu, Y. Zheng and S.-Z. Qiao, *J. Am. Chem. Soc.*, 2021, **143**, 5201–5211.
- 187 S. Chen, N. Zhang, C. W. Narváez Villarrubia, X. Huang, L. Xie, X. Wang, X. Kong, H. Xu, G. Wu, J. Zeng and H.-L. Wang, *Nano Energy*, 2019, **66**, 104164.
- 188 X. Zhang, S. Zhang, Y. Yang, L. Wang, Z. Mu, H. Zhu, X. Zhu, H. Xing, H. Xia, B. Huang, J. Li, S. Guo and E. Wang, *Adv. Mater.*, 2020, **32**, 1906905.
- 189 F. Jaouen, M. Lefèvre, J.-P. Dodelet and M. Cai, *J. Phys. Chem. B*, 2006, **110**, 5553–5558.
- 190 F. Jaouen, J. Herranz, M. Lefèvre, J.-P. Dodelet, U. I. Kramm, I. Herrmann, P. Bogdanoff, J. Maruyama, T. Nagaoka, A. Garsuch, J. R. Dahn, T. Olson, S. Pylypenko, P. Atanassov and E. A. Ustinov, *ACS Appl. Mater. Interfaces*, 2009, **1**, 1623–1639.
- 191 H.-W. Liang, W. Wei, Z.-S. Wu, X. Feng and K. Müllen, *J. Am. Chem. Soc.*, 2013, **135**, 16002–16005.
- 192 Z. Yang, Y. Wang, M. Zhu, Z. Li, W. Chen, W. Wei, T. Yuan, Y. Qu, Q. Xu, C. Zhao, X. Wang, P. Li, Y. Li, Y. Wu and Y. Li, *ACS Catal.*, 2019, **9**, 2158–2163.
- 193 M. Qiao, Y. Wang, Q. Wang, G. Hu, X. Mamat, S. Zhang and S. Wang, *Angew. Chem., Int. Ed.*, 2020, **59**, 2688–2694.
- 194 S. Fu, C. Zhu, D. Su, J. Song, S. Yao, S. Feng, M. H. Engelhard, D. Du and Y. Lin, *Small*, 2018, **14**, 1703118.
- 195 T. Sun, S. Zhao, W. Chen, D. Zhai, J. Dong, Y. Wang, S. Zhang, A. Han, L. Gu, R. Yu, X. Wen, H. Ren, L. Xu, C. Chen, Q. Peng, D. Wang and Y. Li, *Proc. Natl. Acad. Sci. U. S. A.*, 2018, **115**, 12692–12697.
- 196 F. Luo, S. Wagner, I. Onishi, S. Selve, S. Li, W. Ju, H. Wang, J. Steinberg, A. Thomas, U. I. Kramm and P. Strasser, *Chem. Sci.*, 2021, **12**, 384–396.
- 197 M. Primbs, Y. Sun, A. Roy, D. Malko, A. Mehmood, M.-T. Sougrati, P.-Y. Blanchard, G. Granozzi, T. Kosmala, G. Daniel, P. Atanassov, J. Sharman, C. Durante, A. Kucernak, D. Jones, F. Jaouen and P. Strasser, *Energy Environ. Sci.*, 2020, **13**, 2480–2500.
- 198 X. Xie, L. Peng, H. Yang, G. I. N. Waterhouse, L. Shang and T. Zhang, *Adv. Mater.*, 2021, **33**, 2101038.
- 199 L. Shang, H. Yu, X. Huang, T. Bian, R. Shi, Y. Zhao, G. I. N. Waterhouse, L.-Z. Wu, C.-H. Tung and T. Zhang, *Adv. Mater.*, 2016, **28**, 1668–1674.
- 200 L. Jiao, R. Zhang, G. Wan, W. Yang, X. Wan, H. Zhou, J. Shui, S.-H. Yu and H.-L. Jiang, *Nat. Commun.*, 2020, **11**, 2831.
- 201 H. Adabi, A. Shakouri, N. Ul Hassan, J. R. Varcoe, B. Zulevi, A. Serov, J. R. Regalbuto and W. E. Mustain, *Nat. Energy*, 2021, **6**, 834–843.
- 202 H. Shen, E. Gracia-Espino, J. Ma, H. Tang, X. Mamat, T. Wagberg, G. Hu and S. Guo, *Nano Energy*, 2017, **35**, 9–16.
- 203 S. Fu, C. Zhu, J. Song, M. H. Engelhard, X. Li, P. Zhang, H. Xia, D. Du and Y. Lin, *Nano Res.*, 2017, **10**, 1888–1895.
- 204 G. Chen, P. Liu, Z. Liao, F. Sun, Y. He, H. Zhong, T. Zhang, E. Zschech, M. Chen, G. Wu, J. Zhang and X. Feng, *Adv. Mater.*, 2020, **32**, 1907399.
- 205 X. Wan, X. Liu, Y. Li, R. Yu, L. Zheng, W. Yan, H. Wang, M. Xu and J. Shui, *Nat. Catal.*, 2019, **2**, 259–268.
- 206 L. Jiao, J. Li, L. L. Richard, Q. Sun, T. Stracensky, E. Liu, M. T. Sougrati, Z. Zhao, F. Yang, S. Zhong, H. Xu, S. Mukerjee, Y. Huang, D. A. Cullen, J. H. Park, M. Ferrandon, D. J. Myers, F. Jaouen and Q. Jia, *Nat. Mater.*, 2021, **20**, 1385–1391.
- 207 S. Liu, M. Wang, X. Yang, Q. Shi, Z. Qiao, M. Lucero, Q. Ma, K. L. More, D. A. Cullen, Z. Feng and G. Wu, *Angew. Chem., Int. Ed.*, 2020, **59**, 21698–21705.
- 208 Q. Wang, Y. Yang, F. Sun, G. Chen, J. Wang, L. Peng, W.-T. Chen, L. Shang, J. Zhao, D. Sun-Waterhouse, T. Zhang and G. I. N. Waterhouse, *Adv. Energy Mater.*, 2021, **11**, 2100219.
- 209 Z.-F. Huang, J. Song, S. Dou, X. Li, J. Wang and X. Wang, *Matter*, 2019, **1**, 1494–1518.
- 210 D. J. Martin, B. Q. Mercado and J. M. Mayer, *Sci. Adv.*, 2020, **6**, eaaz3318.

